nature communications

Article

https://doi.org/10.1038/s41467-025-57180-3

The role of Tyr34 in proton coupled electron transfer and product inhibition of manganese superoxide dismutase

Received: 28 May 2024

Accepted: 14 February 2025

Published online: 22 February 2025

Check for updates

Jahaun Azadmanesh[1], Katelyn Slobodnik[1], Lucas R. Struble[1], Jeffrey J. Lovelace[1], Erika A. Cone[1], Medhanjali Dasgupta[1], William E. Lutz[1], Siddhartha Kumar[1], Amarnath Natarajan[1], Leighton Coates[2], Kevin L. Weiss[3], Dean A. A. Myles[3], Thomas Kroll[4] & Gloria E. O. Borgstahl[1]

Human manganese superoxide dismutase (MnSOD) plays a crucial role in controlling levels of reactive oxygen species (ROS) by converting superoxide ($O_2^{\bullet-}$) to molecular oxygen (O_2) and hydrogen peroxide (H_2O_2) with proton-coupled electron transfers (PCETs). A key catalytic residue, Tyr34, determines the activity of human MnSOD and also becomes post-translationally inactivated by nitration in various diseases associated with mitochondrial dysfunction. Tyr34 has an unusual pK_a due to its proximity to the Mn metal and undergoes cyclic deprotonation and protonation events to promote the electron transfers of MnSOD. Neutron diffraction, X-ray spectroscopy, and quantum chemistry calculations in oxidized, reduced and product inhibited enzymatic states shed light on the role of Tyr34 in MnSOD catalysis. The data identify the contributions of Tyr34 in MnSOD activity that support mitochondrial function and give a thorough characterization of how a single tyrosine modulates PCET catalysis. Product inhibition occurs by an associative displacement mechanism.

About 25% of known enzymes perform redox reactions to promote cellular functions[1]. These enzymes, known as oxidoreductases, use proton-coupled electron transfers (PCETs)[1–3]. PCETs are required for a wide range of biological functions, including energy generation and DNA synthesis, and oxidoreductase dysfunction leads to many disease states[4–8]. While PCETs are a fundamental biochemical reaction, how they are facilitated by enzymes is not well understood due to difficulties in unraveling the precise proton transfer and electron transfer steps[2,9,10]. Some enzymes use multiple proton transfers per electron transfer step or vice-versa[11–13]. Defining how PCET reactions occur in oxidoreductases benefits the understanding of redox-mediated disease states and furthers therapeutic interventions[14–18].

Some oxidoreductases use their PCETs to regulate the concentrations of reactive oxygen species (ROS) in cells. These PCETs are crucial as fluctuations of ROS levels stimulate mitophagy and programmed cell death, and excessive levels lead to the damage of DNA, proteins, and lipids[19]. Impairment of oxidoreductase function promotes several diseases, including cardiovascular and neurological conditions and cancer progression[20,21]. In particular, the oxidoreductase human manganese superoxide dismutase (MnSOD) is responsible for eliminating superoxide ($O_2^{\bullet-}$) in the mitochondrial matrix. MnSOD dysfunction contributes to a broad range of diseases including psoriasis, inflammatory bowel disease, multiple sclerosis, cardiovascular disease[22], and breast and prostate cancer[23–26]. Overall, the PCETs of MnSOD contribute to health and longevity[27,28]. $O_2^{\bullet-}$ is

[1]Eppley Institute for Research in Cancer and Allied Diseases, 986805 Nebraska Medical Center, Omaha, NE, USA. [2]Second Target Station, Oak Ridge National Laboratory, 1 Bethel Valley Road, Oak Ridge, TN, USA. [3]Neutron Scattering Division, Oak Ridge National Laboratory, 1 Bethel Valley Road, Oak Ridge, TN, USA. [4]Stanford Synchrotron Radiation Lightsource, SLAC National Accelerator Laboratory, Menlo Park, CA, USA. e-mail: gborgstahl@unmc.edu

endogenously produced as a byproduct of the mitochondrial electron transport chain, and MnSOD is the only means to reduce $O_2^{\bullet-}$ in the mitochondrial matrix[29,30].

Within the mitochondrial matrix, MnSOD uses PCETs to decrease $O_2^{\bullet-}$ concentrations rapidly and efficiently ($k_{cat}/K_m > \sim 10^9\,M^{-1}\,s^{-1}$). In the first half-reaction, $O_2^{\bullet-}$ is oxidized to molecular oxygen (O_2) with a Mn^{3+} ion (k_1), and in the second half-reaction, $O_2^{\bullet-}$ is reduced to hydrogen peroxide (H_2O_2) with a Mn^{2+} ion (k_2). The two half-reactions regenerate the Mn^{3+} ion[28].

$$Mn^{3+} + O_2^{\bullet-} \leftrightarrow Mn^{2+} + O_2 \quad k_1 = 1.5\,nM^{-1}s^{-1} \tag{1}$$

$$Mn^{2+} + O_2^{\bullet-} + 2H^+ \leftrightarrow Mn^{3+} + H_2O_2 \quad k_2 = 1.1\,nM^{-1}s^{-1} \tag{2}$$

For PCET catalysis, MnSOD uses a hydrogen bond network (dashed blues lines, Fig. 1a right panel) to couple proton transfers with changes in Mn oxidation state[28,31,32]. The Mn ion is covalently bound to His26, His74, His163, Asp159, and a solvent molecule called WAT1. From WAT1, the hydrogen bond network extends to Asp159, Gln143, Tyr34, WAT2, His30, and Tyr166 from the adjacent subunit. To enter the active site, the substrate and solvent pass through a gateway formed by Tyr34 and His30. The distance between Tyr34(O^H) and His30($N^{\delta1}$) is 5.4 Å. Hydrophobic residues Trp123, Trp161, and Phe66 hold the hydrogen bonding atoms of Asp159, WAT1, Gln143, and Tyr34 close together[33]. In our previous work, we investigated the protonation states of the hydrogen bond network in relation to the oxidation state of the Mn ion[13].

Using neutron crystallography, we previously observed how changing the Mn oxidation state shifts the pK_a of active site amino acids and leads to several unusual protonation states[13]. Neutron diffraction is advantageous for studying PCET mechanisms because the scattering of deuterium is on par with carbon, nitrogen, and oxygen, and neutrons do not photoreduce metal ions, unlike X-rays[34,35]. The neutron structures of Mn^{3+}SOD and Mn^{2+}SOD revealed three important observations on how PCET catalysis is facilitated. First, during the Mn^{3+} to Mn^{2+} redox transition, an unconventional proton transfer occurs between Gln143 and metal-bound $^-$OH(WAT1), leading to an unusual Gln143 amide anion and H_2O (Fig. 1b). The amide anion is stabilized by two short-strong hydrogen bonds (SSHBs) with WAT1 and Trp123. SSHBs stabilize catalytic steps and enhance kinetic rates (hashed lines, Fig. 1b)[36–38]. Second, the $N^{\delta1}$ of His30 is protonated only in the Mn^{2+} oxidation state (Fig. 1c) and a low-barrier hydrogen bond (LBHB) is formed between Tyr166 and His30 in the Mn^{2+} state. A LBHB is a type of SSHB where the heteroatoms transiently share a proton, and the hydrogen bond distances are nearly equivalent (1.2–1.3 Å)[39]. Third, Tyr34 is deprotonated in the Mn^{3+} oxidation state and becomes protonated in the Mn^{2+} state (Fig. 1d). We concluded that Tyr34 and His30 are probably the two proton donors needed during the Mn^{2+} to Mn^{3+} redox transition to form H_2O_2 from the protonation of $O_2^{\bullet-}$ (k_2)[28,32,40,41]. Overall, the previous MnSOD neutron structures indicate that multiple proton transfers are coupled to electron transfer events and that the active site metal leads to residues with unconventional pK_as essential for PCET catalysis.

How $O_2^{\bullet-}$ interacts with the active site for catalysis is unclear[28,31,32]. $O_2^{\bullet-}$ may bind the Mn ion directly for an inner-sphere electron transfer or between His30 and Tyr34 for a long-range outer-sphere electron transfer with the Mn ion[28,31,32,41]. The inner sphere binding site for $O_2^{\bullet-}$ is unknown and could form a six or five coordinate active site binding. The sixth site is predicted to bind opposite Asp159[42]. Five coordinate binding would displace Asp159 or WAT1[43]. Quantum chemistry computational studies have postulated that the first half-reaction (k_1, Mn^{3+} → Mn^{2+}) proceeds through an inner-sphere electron transfer while the second half-reaction (k_2, Mn^{2+} → Mn^{3+}) proceeds through an outer-sphere electron transfer[41]. The outer-sphere mechanism for the second half-reaction is a promising hypothesis because His30 and Tyr34 have been shown to lose protons during the Mn^{2+} → Mn^{3+} redox transition (Fig. 1c, d)[13]. His30 and Tyr34 could protonate $O_2^{\bullet-}$ in concert with long-range electron transfer to form the H_2O_2 product. While there is no structural evidence for how $O_2^{\bullet-}$ interacts with the active site for electron transfer, modeling, and quantum chemical calculations support the second half-reaction proceeding through an outer-sphere mechanism[41].

Human MnSOD is inhibited by its product, H_2O_2, to regulate the output of mitochondrial H_2O_2. Physiologically, MnSOD product inhibition is thought to be related to H_2O_2 acting as a second messenger[31,32,44]. Mitochondrially-derived H_2O_2 plays a role in apoptosis[45,46], mitochondrial biogenesis[44], and protein localization and activity[47]. Furthermore, mitochondrial H_2O_2 has been shown to modulate the activity of PTEN (phosphatase and tensin homolog), a protein tyrosine phosphatase that contributes to cancer and neurological disease[48,49]. Mitochondrial H_2O_2 may also be scavenged by peroxiredoxins (PRDXs) and glutathione peroxidases (GPXs). These enzymes are dependent on nicotinamide adenine dinucleotide phosphate (NADPH) for function[50–52]. MnSOD product inhibition regulates mitochondrial H_2O_2 levels independent of metabolic status. However, little is known about how MnSOD mechanistically achieves product inhibition.

Product inhibition occurs when the ratio of $O_2^{\bullet-}$ to MnSOD is high[31,32]. At concentrations of $O_2^{\bullet-}$ that are lower than enzyme, catalysis proceeds rapidly through the first-order reactions k_1 and k_2. At concentrations of $O_2^{\bullet-}$ that are much greater than enzyme, catalysis proceeds through the reversible inhibition reactions k_3 (first-order) and k_4 (zero-order). The k_3 reaction forms a product-inhibited complex (indicated by square brackets) that is unreactive to $O_2^{\bullet-}$ and only dissociates through the zero-order k_4 reaction that dictates the lifetime of the complex. Several kinetic models suggest that inhibition is initiated from the reaction of a Mn^{2+} ion with $O_2^{\bullet-}$ in the absence of protonation to form [Mn^{3+}-O_2^{2-}] or [Mn^{3+}-$^-$OOH] (k_3)[31,32]. The inhibited complex is then relieved by at least one protonation to yield Mn^{3+} and H_2O_2 (k_4). Since k_2 and k_3 both use Mn^{2+} and $O_2^{\bullet-}$ as reactants, they are competing reactions, and their ratios determine the propensity for MnSOD to become product-inhibited. Human MnSOD has equal k_2 and k_3 (Supplementary Table 1), which means at high $O_2^{\bullet-}$ to enzyme ratios, ~50% of Mn^{2+} reactions with $O_2^{\bullet-}$ form the inhibited complex[53,54]. The factors that govern k_3 and k_4 are unclear, although Tyr34 appears to contribute to the inhibition process[55,56].

$$Mn^{2+} + O_2^{\bullet-} \leftrightarrow [Mn^{3+} - O_2^{2-}] \quad k_3 = 1.1\,nM^{-1}s^{-1} \tag{3}$$

$$[Mn^{3+} - O_2^{2-}] + 2H^+ \leftrightarrow Mn^{3+} + H_2O_2 \quad k_4 = 120\,s^{-1} \tag{4}$$

or

$$Mn^{2+} + O_2^{\bullet-} + H^+ \leftrightarrow [Mn^{3+} - {}^-OOH] \quad k_3 = 1.1\,nM^{-1}\,s^{-1} \tag{5}$$

$$[Mn^{3+} - {}^-OOH] + H^+ \leftrightarrow Mn^{3+} + H_2O_2 \quad k_4 = 120\,s^{-1} \tag{6}$$

Tyr34 is a conserved residue in the active site of MnSOD[55,57]. Physiologically, the residue becomes nitrated in several human neurodegenerative diseases, leading to inactivated MnSOD[58]. During the PCET mechanism, Tyr34 is thought to be one of the sources of protons needed to produce H_2O_2 during the Mn^{2+} to Mn^{3+} redox transition[28,32,57]. Our previous neutron structures show that Tyr34 is poised to donate a proton in Mn^{2+}SOD (Fig. 1d)[13]. Interestingly, the Tyr34Phe MnSOD variant is unable to proceed through the fast Mn^{2+} to Mn^{3+} redox transition (k_2), and catalysis proceeds exclusively through the product-inhibited pathway k_3 (see rate constants listed in Supplementary

https://doi.org/10.1038/s41467-025-57180-3

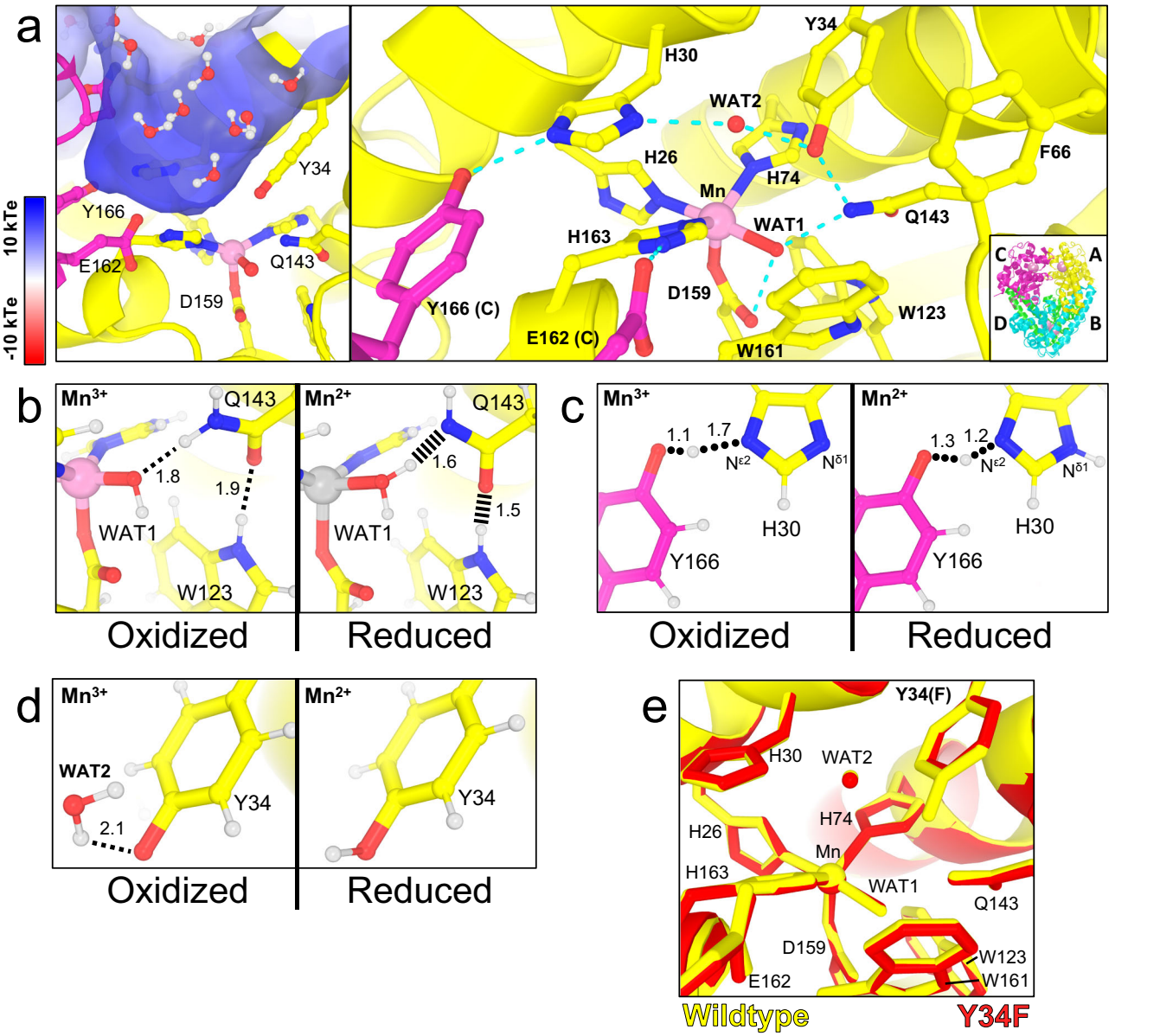

Fig. 1 | Structure of human wildtype MnSOD and protonation differences between oxidation states. a The active sites of tetrameric MnSOD are found in positively charged cavities made by two subunits. Solvent and substrate must pass through gateway residues His30 and Tyr34 to interact with the catalytic Mn ion. The distance between Tyr34(O^H) and His30($N^{\delta1}$) is 5.4 Å. Blue dashed lines indicate hydrogen bonds. The inset indicates the chain identity derived crystallographically, where the asymmetric unit is composed of an AB dimer, and the CD dimer is generated through symmetry to form the native tetrameric assembly. **b** Room temperature neutron structures revealed changes in protonation among WAT1 and Gln143 and alterations in the hydrogen bond network of WAT1-Gln143-Trp123. Dotted lines indicate hydrogen bonds ≥ 1.8 Å while hashed lines indicate SSHBs that are hydrogen bonds < 1.8 Å. **c** A shared proton, indicated with rounded dots, was observed between His30 and Tyr166. This proton helps modulate the protonation state of $N^{\delta1}$(His30) when the Mn ion changes oxidation states. **d** Tyr34 is deprotonated in Mn^{3+}SOD and protonated in Mn^{2+}SOD. There is no water within hydrogen bond distance on Tyr34 in Mn^{2+}SOD. **e** Superposition of wildtype MnSOD (yellow, PDB ID 5VF9) and Tyr34Phe MnSOD (red, PDB ID 9BWR) active sites with a root-mean-square deviation of 0.07 Å among C^{α} atoms. Panel **a** was created from MnSOD X-ray structure (PDB ID 5VF9)[70], and panels (**b**–**d**) were created from the neutron structures of Mn^{3+}SOD (PDB ID 7KKS) and Mn^{2+}SOD (PDB ID 7KKW)[13]. All hydrogen positions were experimentally determined except for solvent molecules in panel **a** that were randomly generated to accentuate the solvent in the active site funnel. All distances are in Å.

Table 1). When $k_2 << k_3$ then ~99% of Mn^{2+} reactions with $O_2^{\bullet-}$ form the inhibited complex. There is also higher retention of the inhibited complex, with half the disassociation rate compared to wildtype (see k_4, Supplementary Table 1). Since the active site structure of the Tyr34Phe variant is practically identical to wildtype (Fig. 1e)[57], the perturbed kinetics and enrichment of product inhibition of the Tyr34Phe variant are probably due to the loss of the hydroxyl group for proton transfer. Interestingly, the Trp161Phe variant, which does not eliminate a hydroxyl group, also primarily uses the product inhibited pathway. In fact, Trp161Phe has similar kinetics to the Tyr34Phe variant (Supplementary Table 1)[33]. This suggests that the contribution of Tyr34 toward catalysis is not solely proton transfer. To study the effects that govern the reactions k_1-k_4 of MnSOD, we performed a series of experiments with the Tyr34Phe variant.

Several studies have reported that mixing high H_2O_2 concentrations with Mn^{3+}SOD leads to the formation of the product-inhibited complex that decays to Mn^{2+}SOD[33,59–61]. Mutagenesis studies found the process to be correlated with the forward reactions k_2-k_4. These

https://doi.org/10.1038/s41467-025-57180-3

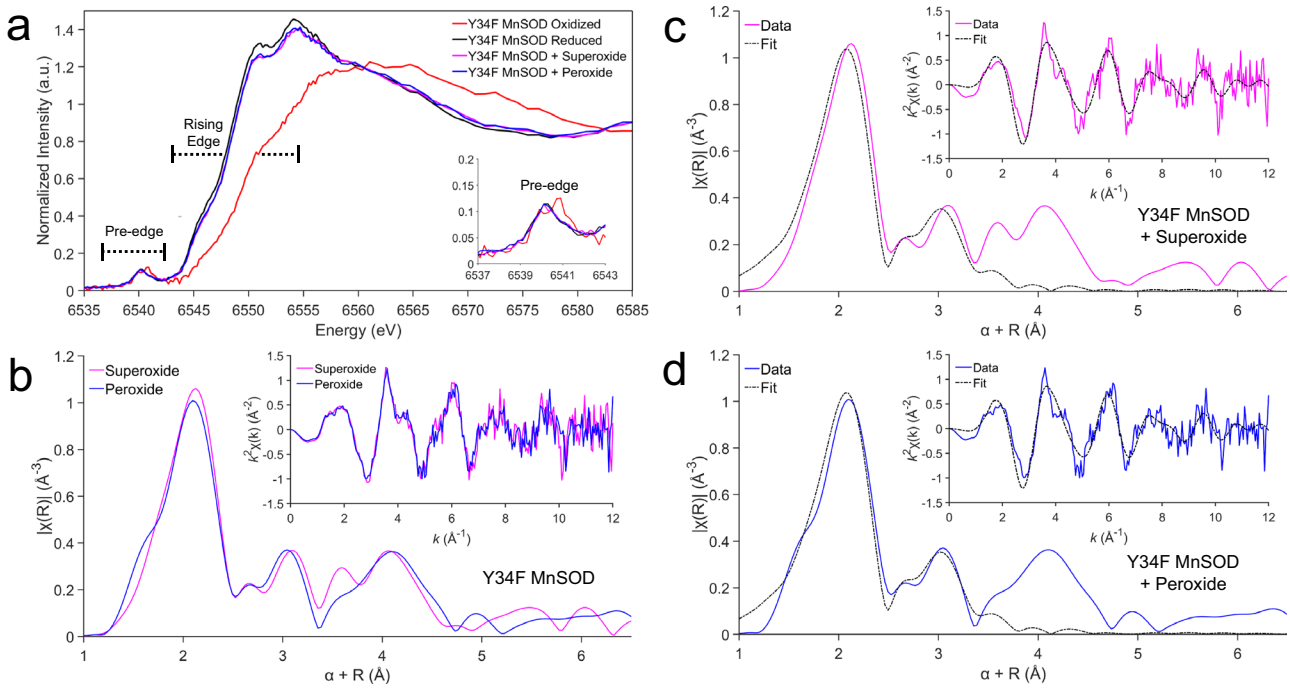

Fig. 2 | High Energy Resolution Fluorescence Detection (HERFD) X-ray Absorption Spectroscopy of Tyr34Phe MnSOD. a The HERFD-XANES region of Tyr34Phe MnSOD treated with potassium dichromate to isolate the Mn^{3+}SOD resting state, sodium dithionite to isolate the Mn^{2+}SOD resting state, and either superoxide or hydrogen peroxide to isolate the product-inhibited state. **b** Overlay of the Fourier transform of Mn K-edge EXAFS data [$k^2\chi(k)$] from superoxide- and peroxide-soaked Tyr34Phe MnSOD with the EXAFs spectrum in *k*-space shown in the inset. Due to the scattering phase shift, the distance found by the Fourier Transformation (R) is ~0.5 Å shorter than the actual distance and a 0.5 Å correction (α) was implemented. **c**, **d** Superoxide- and peroxide-soaked Tyr34Phe MnSOD with the EXAFs spectrum. Colored lines represent experimental data, while the black line is simulated EXAFS spectra fit to the experimental data.

puzzling results may be explained by excessive concentrations of H_2O_2 initiating a backward reaction with Mn^{3+}SOD to produce $O_2^{\bullet-}$, and then a subsequent forward reaction of $O_2^{\bullet-}$ with MnSOD to form the inhibited complex[60,61]. Importantly, this would provide an avenue to structurally analyze product inhibition without relying on volatile $O_2^{\bullet-}$ solutions[62]. We combined H_2O_2 soaking with the Tyr34Phe variant to study the product-inhibited complex and gain new information on the MnSOD PCET mechanism and an enhanced understanding of product inhibition.

To help understand the role of the hydroxyl group of Tyr34 in MnSOD activity we used the Tyr34Phe MnSOD variant in combination with neutron crystallography, X-ray absorption spectroscopy (XAS), and quantum mechanical (QM) chemistry calculations. With neutron crystallography, we captured the product-bound, reduced, and oxidized states of Tyr34Phe MnSOD free from radiation-induced perturbations. For each state, we used XAS to determine the oxidation state and coordination number of the manganese with each treatment, and to probe the electron orbitals of the Mn ion. Solution XAS data was useful in guiding the interpretation of neutron crystal structures that sometimes have asymmetric active site structures between subunits due to the crystal lattice. Then, we used QM calculations to quantitatively interrogate the Mn ion orbitals that determine redox activity. Lastly, the Tyr34Phe data were compared with wildtype[13] and Trp161Phe[63] to piece together a MnSOD mechanism that describes the reactions k_1-k_4. With respect to oxidoreductases in general, our work presents a thorough characterization of how a single tyrosine modulates PCET catalysis. Our main finding is that Tyr34 plays a part in every MnSOD kinetic step: proton donor/acceptor, orienting nearby residues for rapid proton transfer, limiting the product inhibited complex, and keeping the lifetime of the inhibited state short. Thus, Tyr34 in MnSOD is a central regulator of H_2O_2 levels in the mitochondria and signaling.

Results and discussion

X-ray absorption spectroscopy (XAS) characterization of Tyr34Phe MnSOD

Tyr34Phe MnSOD was selected for this study to help understand the role of Tyr34's hydroxyl group on the MnSOD PCET and product inhibition mechanisms. Solution XAS data is useful in guiding the interpretation of neutron crystal structures. In Mn K-edge XAS, the X-ray absorption near edge structure (XANES) contains information on the oxidation and coordination states of the Mn, while the extended X-ray absorption fine structure (EXAFS) region provides information on Mn-ligand bond distances. The Tyr34Phe MnSOD variant is advantageous in this study because it accumulates and retains the product-inhibited complex, and from that, we can infer information about the PCET mechanism (see Supplementary Table 1 for rate constants). First, we measured the XANES spectral signature to characterize four states of Tyr34Phe MnSOD: oxidized, reduced, H_2O_2 soaked, and $O_2^{\bullet-}$ soaked (see Supplementary Fig. 2 for all Tyr34Phe, Trp161Phe and WT MnSOD HERFD-XANES spectra, and structural comparisons).

The energy of the rising edge of the XANES region increases with higher oxidation states, while the intensity of the pre-edge contains information about the coordination of the Mn ion (Fig. 2a). The pre-edge corresponds to 1 s to 3 d orbital transitions, with gains in intensity from 4p character mixing into the 3 d orbitals from symmetry distortions and/or loss of inversion symmetry[64–66]. Based on electron paramagnetic resonance (EPR) data, the Mn ion is expected to be high-spin in both Mn^{3+} and Mn^{2+} states[67]. For oxidized Tyr34Phe MnSOD, the rising edge is observed at higher energy than the reduced data, indicating a difference in the Mn ion valency. Given that these samples were mixed with stoichiometric excesses of redox reagents, we interpret oxidized Tyr34Phe MnSOD as Mn^{3+} and reduced Tyr34Phe MnSOD as Mn^{2+}. For both oxidized and reduced Tyr34Phe MnSOD, the pre-edge intensity (i.e., the area under the curve, inset Fig. 2a)

https://doi.org/10.1038/s41467-025-57180-3

Table 1 | Comparison of superoxide and peroxide-soaked Tyr34Phe MnSOD bond distances found through EXAFS fitting, neutron crystallography, and DFT calculations

Exp.	EXAFS (Å) Y34F MnSOD + Superoxide	EXAFS (Å) Y34F MnSOD + Peroxide	Neutron Structure (Å) Y34F MnSOD + Peroxide
Mn-$N^{\varepsilon 2}$(H26)	2.15	2.15	2.17
Mn-$N^{\varepsilon 2}$(H74)	2.15	2.15	2.23
Mn-$N^{\varepsilon 2}$(H163)	2.15	2.15	2.21
Mn-$O^{\delta 2}$(D159)	2.11	2.11	2.13
Mn-O^{1}(LIG)	2.11	2.11	2.00
Mn-O^{2}(LIG)[a]	2.44	2.44	2.34
Calc.	**DFT (Å) Y34F Mn^{2+}SOD + $^{-}O_2H$**	**DFT (Å) Y34F Mn^{3+}SOD + $^{-}O_2H$**	**DFT (Å)[b] Y34F Mn^{2+}SOD + $^{\bullet}O_2H$**
S	5/2	2	3
Mn-$N^{\varepsilon 2}$(H26)	2.28 (0.11)	2.00 (0.17)	2.12 (0.05)
Mn-$N^{\varepsilon 2}$(H74)	2.20 (0.03)	2.07 (0.16)	2.16 (0.07)
Mn-$N^{\varepsilon 2}$(H163)	2.16 (0.03)	2.19 (0.06)	2.17 (0.04)
Mn-$O^{\delta 2}$(D159)	2.17 (0.04)	2.01 (0.12)	2.01 (0.12)
Mn-O^{1}(LIG)	2.10 (0.10)	1.82 (0.18)	2.37 (0.37)
Mn-O^{2}(LIG)[a]	2.38 (0.04)	2.60 (0.26)	3.03 (0.69)

[a]The second oxygen of the dioxygen ligand is not directly bound to the Mn ion.
[b]Broken-symmetry geometry optimization of Mn^{2+}-$^{\bullet}O_2H$ with S = 2 collapses to a Mn^{3+}-$^{-}O_2H$ complex.
[c]The absolute value of the difference between the neutron structure bond length and the DFT bond length are given in parenthesis.

corresponds to a distorted five-coordinate trigonal bipyramidal complex that has been observed in crystal structures[57,68]. A strong pre-edge intensity requires electric dipole allowed transitions that can only occur due to the presence of Mn 4p character mixed into the 3 d orbitals. Such a mixing requires the absence a local inversion center around the Mn ion as is the case for a 5-coordinated complex. For a 6-coordinated complex, a sufficient amount of 4p character could only be reached by one short Mn-ligand bond distance, as it is observed for example for some Fe-O complexes[66]. However, neither our neutron scattering, XAS or DFT data suggest such a geometry.

To isolate the product-inhibited complex with XAS, we introduced $O_2^{\bullet -}$ or H_2O_2 to Tyr34Phe MnSOD. $O_2^{\bullet -}$ was used to isolate the complex from the forward reaction and H_2O_2 was used to attain the complex with the back reaction[60,61]. For both approaches, the inhibited complex has been reported to form within 44 ms of mixing with Tyr34Phe MnSOD[60]. Indeed, the approaches yield nearly identical XANES spectra and reveal that the same electronic structure is formed (Fig. 2a). The superoxide and peroxide-soaked spectra are like Tyr34Phe Mn^{2+}SOD, indicating the presence of a divalent Mn ion. However, these spectra have unique features relative to Tyr34Phe Mn^{2+}SOD, with lower intensities at ~6550-6555 eV and higher intensities at ~6565-6575 eV. Similarly, the pre-edge intensities are like Tyr34Phe Mn^{2+}SOD to indicate that the resulting complex from either mixing $O_2^{\bullet -}$ or H_2O_2 is five-coordinate (Fig. 2a). Altogether, by using the Tyr34Phe MnSOD variant that enriches for the product-inhibited complex, we show that an electronically distinct five-coordinate Mn^{2+} complex forms from either exposure to $O_2^{\bullet -}$ or H_2O_2.

Next, we investigated the EXAFS region of the $O_2^{\bullet -}$ and peroxide-soaked Tyr34Phe MnSOD K-edge spectra. The Fourier transform of the EXAFS data, $\chi(k)$, yields $\chi(R)$ that provides information on the atomic radial distribution (bond lengths) around the absorbing Mn ion (Fig. 2b–d). Overall, the k-space (inset) and R-space spectra are highly similar for $O_2^{\bullet -}$ and H_2O_2 soaked Tyr34Phe MnSOD and yield the same Mn bond distance solutions (Table 1). For both samples, the first shell of coordination observed at ~2.1 Å is best fit by three N atoms at 2.15 Å and two O atoms at 2.11 Å to indicate a five-coordinate complex (Supplementary Table 2 and 3). These account for $N^{\varepsilon 2}$ atoms of His26, His74, and His163, $O^{\delta 2}$ atom of Asp159, and another O atom (denoted O^1). As the next closest scatterer is a single atom found at 2.44 Å (denoted O^2), we interpret O^1 and O^2 as belonging to a dioxygen species. The largest contributors to the second peak seen at ~3.0 Å are seven carbon atoms that correspond to the $C^{\delta 2}$ and $C^{\varepsilon 1}$ of the three histidines and the C^{γ} of the aspartate residue. Overall, the EXAFS data show that when $O_2^{\bullet -}$ or H_2O_2 are given to Tyr34Phe MnSOD, a five-coordinate Mn complex that includes a dioxygen species is formed.

Our XAS data indicate that H_2O_2 has both a reducing effect on MnSOD and can form the inhibited complex. The reducing effect of MnSOD by H_2O_2 has been reported previously[59,60]. Thermodynamically, the process is unfavorable as the reduction potential of wildtype Mn^{3+}SOD to Mn^{2+}SOD is 0.4 V, and the oxidation potential of H_2O_2 to $O_2^{\bullet -}$ is -0.85 V[69]. However, a 100-fold excess of H_2O_2 was used, probably driving a backward reaction[60,61]. Mutagenesis studies have indicated that forming the inhibited complex through peroxide-soaking depends on reactions k_2-k_4 and suggests that the $O_2^{\bullet -}$ generated from the backward reaction then reacts with MnSOD in the forward direction[60]. In these past experiments, detection of $O_2^{\bullet -}$ was lost during the dead time of the instrument (1.4 ms). As H_2O_2 is more stable than $O_2^{\bullet -}$ in aqueous solution, we used H_2O_2 for the structural studies on Tyr34Phe MnSOD.

Neutron structure of the Tyr34Phe product-inhibited complex

To visualize the product-inhibited complex and the corresponding active site protonation states, we solved a cryocooled neutron structure of perdeuterated Tyr34Phe MnSOD soaked with deuterium peroxide (D_2O_2) at 2.30 Å resolution. For the neutron structures, proton positions can be assigned at 2.5 Å or better. We first solved the all-atom structure of the entire enzyme, excluding the active site. Then, with these phases, we carefully interrogated the active site nuclear density maps for the active site coordination and protonation states.

For chain A, the omit $|F_o| - |F_c|$ nuclear scattering-length density next to the Mn ion was oblong at 3.0 σ (Fig. 3a). We interpreted the density as a dioxygen species with a single proton (denoted as LIG for ligand) that has taken the place of the WAT1 position observed in the resting states (Fig. 1b). The proton of LIG, D^2, points toward Trp161 and appears to be interacting with the pi system (Fig. 3a). The O^2(LIG) and $D^{\varepsilon 21}$(Gln143) atoms are close in proximity (2.2 Å apart) though LIG and Gln143 are not in optimal geometry for hydrogen bonding (Figs. 3a, b and Supplementary Fig. 1a). LIG refined well at full occupancy and led to Mn bond distances that closely resemble those measured from the EXAFS spectra (Table 1). At physiological temperatures, optical absorption spectra in the literature also suggest a displacement of WAT1 and binding of a dioxygen species, which agrees with our cryocooled diffraction data[43]. For chain B, the omit $|F_o| - |F_c|$ is instead a spherical shape at 3.0 σ (Supplementary Fig. 1b), indicating a $^{-}$OD molecule that has been previously observed in wildtype neutron structures[13]. Contrasting structures between the two subunits of the asymmetric unit are often observed for the MnSOD $P6_122$ crystal form due to differences in solvent accessibility[13,70]. In chain B, the six-coordinate nuclear density near the Mn ion and $^{-}$OD molecule did not correspond with the five-coordinate XAS data, making it less useful in terms of defining the PCET mechanism (Supplementary Fig. 1b). Regardless, from the nuclear density at chain A, a singly protonated dioxygen species replaces WAT1 upon D_2O_2 soaking and forms a complex with bond distances like those found from EXAFS spectra (Table 1).

https://doi.org/10.1038/s41467-025-57180-3

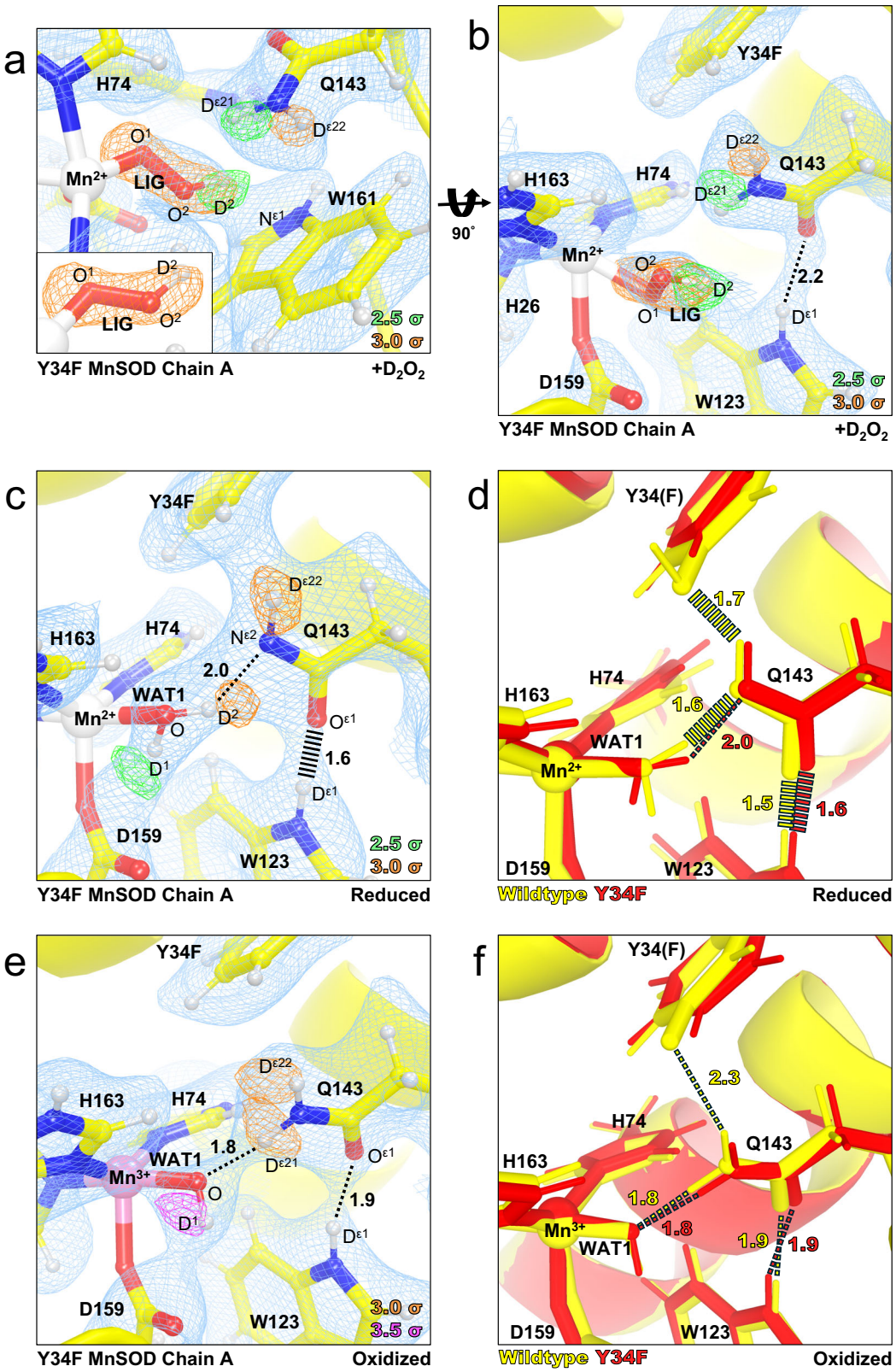

Fig. 3 | Neutron structures and protonation states at the active site of D_2O_2-soaked, reduced, and oxidized Tyr34Phe MnSOD. a D_2O_2-soaked Tyr34Phe MnSOD for chain A with a singly-protonated dioxygen species denoted LIG. The inset highlights the elongated $|F_o| - |F_c|$ difference density of LIG. **b** D_2O_2-soaked Tyr34Phe MnSOD for chain A rotated 90° along the horizontal axis relative to panel (**a**). **c** Tyr34Phe Mn^{2+}SOD for chain A. *Notably, this neutron structure is the lowest resolution, 2.5 Å of the three in* Supplementary Table 6. **d** Active site overlay of wildtype Mn^{2+}SOD (PDB 7KKW, solved at 2.3 Å resolution) and Tyr34Phe Mn^{2+}SOD (this study, solved at 2.5 Å resolution). **e** Tyr34Phe Mn^{3+}SOD for chain A. **f** Active site overlay of wildtype Mn^{3+}SOD (PDB 7KKS, solved at 2.3 Å resolution) and Tyr34Phe Mn^{3+}SOD (this study, solved at 2.3 Å resolution). Green, orange, and magenta omit $|F_o| - |F_c|$ difference neutron scattering length density of protons displayed at 2.5σ, 3.0σ, and 3.5σ. respectively. Light blue $2|F_o| - |F_c|$ density is displayed at 1.0σ. Distances are in Å. Dashed lines indicate hydrogen bonds ≥ 1.8 Å, and hashed lines indicate SSHBs that are hydrogen bonds < 1.8 Å. Chain B active sites are shown in Supplementary Fig. 1.

How the product-inhibited complex is formed as well as its oxidation state and coordination, have been historically controversial[31,32,61,71–73]. The generally accepted mechanism is that inhibition is initiated from $O_2^{\bullet-}$ binding Mn^{2+} to form a Mn^{3+}-O_2^{2-} complex (k_3, Supplementary Table 1)[28,31,32,74,75]. Our XAS data indicates a five-coordinate Mn^{2+} as the identity of the complex[59,60]. Indeed, the neutron structure of Tyr34Phe MnSOD soaked with D_2O_2 yields a five-coordinated active site with a singly-protonated dioxygen species. The Mn bond distances of the solved neutron structure with Mn^{2+} and a hydroperoxyl anion, ^-O_2H, resemble those from the EXAFS data. Also, the density function theory (DFT) calculations using Mn^{2+} and ^-O_2H most closely match the neutron structure (Table 1). Overall, these data and calculations indicate that the inhibited complex is a five-coordinate Mn^{2+} complex where the WAT1 position has been replaced with ^-O_2H.

Tyr34 orients the Gln143-WAT1 SSHB of Mn^{2+}SOD and limits product inhibition

We next wondered whether enrichment of the product-inhibited complex in the Tyr34Phe variant was because of structural perturbations near the Mn ion or due to the absence of the Tyr34 hydroxyl group for proton transfer. To this end, we solved neutron structures of reduced and oxidized Tyr34Phe MnSOD at 2.5 and 2.3 Å resolution, respectively. For reduced Tyr34Phe MnSOD, the Mn bond distances are similar to five-coordinate wildtype Mn^{2+}SOD (Supplementary Table 4). Furthermore, the protonation states resemble those of wildtype Mn^{2+}SOD, where WAT1 is of the D_2O form while Gln143 is deprotonated to the amide anion (Fig. 3c). Deprotonated amino acids are identified when attempts to model and refine a proton result in negative $|F_o| - |F_c|$ difference neutron scattering length density, and all the other protons of the amino acid can be placed. Interestingly, the lack of the hydroxyl group in Tyr34Phe Mn^{2+}SOD perturbs the orientation of Gln143 and lengthens the WAT1-Gln143 hydrogen bond (Fig. 3d). The WAT1-Gln143 SSHB of the wildtype enzyme is critical for the back-and-forth proton transfers needed for redox cycling of the Mn ion[13], and the Tyr34Phe Mn^{2+}SOD neutron structure suggests one role Tyr34 plays in catalysis is correctly positioning Gln143 for rapid PCET catalysis. Indeed, the Mn^{2+} to Mn^{3+} redox transition is greatly diminished for Tyr34Phe MnSOD (k_2, Supplementary Table 1)[31,32]. Another consequence of the perturbation of the WAT1-Gln143 interaction is the potentially easier displacement of WAT1 by a dioxygen species to form the product-inhibited complex. Overall, the reduced Tyr34Phe MnSOD neutron structure suggests that Tyr34 orients Gln143 for a tight hydrogen bonding interaction with WAT1.

For oxidized Tyr34Phe MnSOD, the Mn ion is like wildtype with a bound $^-$OD molecule (Fig. 3e) with similar covalent bond distances (Supplementary Table 4), and identical hydrogen bond distances for O(WAT1)-$D^{\varepsilon 21}$(Gln143) and $D^{\varepsilon 1}$(Trp123)-$O^{\varepsilon 1}$(Gln143) (Fig. 3f). As PCET mechanisms depend on the distribution of electrostatic vectors to propagate proton and electron transfers, the missing anionic deprotonated Tyr34 in this variant probably perturbs enzyme kinetics. Such electronic effects are indicated by the lower kinetic rates of the Mn^{3+} to Mn^{2+} redox transition for the Tyr34Phe variant (k_1, Supplementary Table 1). Overall, the interactions between WAT1, Gln143, and Trp123 are the same in Tyr34Phe and wildtype Mn^{3+}SOD making this variant. Because these active sites are practically identical the use of Tyr34Phe MnSOD and its handy kinetic data to study the product inhibited state is valid and can help interpret the wildtype mechanism.

The neutron structures of reduced and oxidized Tyr34Phe Mn^{2+}SOD suggest the roles of Tyr34 in catalysis are (1) orient Gln143 for efficient interaction and proton transfer with WAT1 during the Mn^{2+} to Mn^{3+} PCET reaction, (2) limit formation of the product-inhibited complex by strengthening the WAT1-Gln143 hydrogen bond, and (3) contribute subtle electronic effects as a phenolate anion during the Mn^{3+} to Mn^{2+} reaction. These interpretations are supported by the kinetic rates of Tyr34Phe MnSOD[31,32]. For Tyr34Phe MnSOD, the fast Mn^{2+} to Mn^{3+} redox reaction is dramatically reduced (k_2, Supplementary Table 1), formation of the product-inhibited complex is enriched ($k_3 >> k_2$, Supplementary Table 1), and the Mn^{3+} to Mn^{2+} redox reaction is cut in third (k_1, Supplementary Table 1). A unifying theme among Tyr34Phe MnSOD and other variants studied kinetically is that the precise orientation of Gln143 is critical for catalysis. Mutating residues directly adjacent to Gln143, such as Trp161, Trp123, and Tyr34, lead to similar kinetic consequences, where the $Mn^{2+} \rightarrow Mn^{3+}$ half reaction is greatly diminished, product inhibition is enriched, and the $Mn^{3+} \rightarrow Mn^{2+}$ half reaction is slower compared to wildtype[31,32]. These redundant effects of the Trp161Phe, Trp123Phe, and Tyr34Phe variants suggest that a crucial role of residues neighboring Gln143 is to enforce a SSHB between WAT1 and Gln143. In the case of Tyr34, our neutron structures indicate that Tyr34 is responsible for positioning Gln143 for a SSHB with WAT1 during the Mn^{2+} resting state and that the strength of the bond between Gln143 and WAT1 correlates with the extent of product inhibition.

Retention of the product-inhibited complex is dependent on the Gln143 position

As the XAS and neutron crystallographic data of Tyr34Phe MnSOD demonstrated the formation of a five-coordinated Mn^{2+}SOD with a singly-protonated dioxygen species replacing the WAT1 position, we wondered if the formation and retention of the inhibited complex could be distinguished with other variants of MnSOD. In the context of Tyr34Phe MnSOD, we also sought to define whether the enrichment of product inhibition was due to the loss of the ionizable Tyr group only or also due to the perturbation of the Gln143-WAT1 SSHB interaction. For example, the Trp161Phe MnSOD variant alters a residue directly adjacent to Gln143 and has enriched product-inhibition kinetics like those of Tyr34Phe MnSOD (Supplementary Table 1)[59]. For wildtype, Tyr34Phe, and Trp161Phe, we performed XANES in the HERFD mode of detection, which allows a large improvement in energy resolution and sensitivity compared to conventional XANES[76–78]. Here, we focused on comparing the reduced form of the variants to those of peroxide-soaked counterparts. As all these complexes are expected to be five-coordinated d^5 with spin S = 5/2, we sought to distinguish fine details of the spectra offered by the HERFD mode of detection (detailed evaluation of these data can be found in the Supplementary Information pages 10-13 and Supplementary Fig. 3). Overall, reduced and peroxide-soaked Tyr34Phe MnSOD spectra had distinct features between each other, and the general shape trends were reproducible with conventional XANES (Fig. 2a) and HERFD-XANES (Supplementary Fig. 3a). Similar trends were observed between reduced and peroxide-soaked forms of Tyr34Phe and Trp161Phe MnSOD (Supplementary Fig. 3ab). Since the wildtype enzyme exhibits physiological product inhibition levels ($k_3 = k_2$), compared to the Tyr34Phe and Trp161Phe variants that are enriched for product inhibition ($k_3 >> k_2$ and lower k_4 compared to wildtype, Supplementary Table 1), a potential explanation for the less pronounced differences for the wildtype pair is that the peroxide-soaked data may reflect a mixture of species rather than a fully isolated product-bound complex (Supplementary Fig. 3c). The XERFD-XANES data for peroxide soaked Y34F, W161F and wild-type are similar and follow these trends (Supplementary Fig. 3d). These observations indicate that retention of the inhibited complex is not exclusively dependent on a proton transfer from Tyr34 but instead on other factors of the active site. We compared our D_2O_2-soaked Tyr34Phe MnSOD neutron structure with that of our previous D_2O_2-soaked Trp161Phe MnSOD neutron structure (Supplementary Fig. 3e, PDB ID 8VHW[63] and concluded that the LIG orientation in Tyr34Phe MnSOD is probably close to what would occur physiologically. When the reduced structures are compared, both variant structures have a lengthened WAT1-Gln143 interaction compared to wildtype (Supplementary Fig. 3f, PDB ID 8VHY)[63]. Altogether, these

https://doi.org/10.1038/s41467-025-57180-3

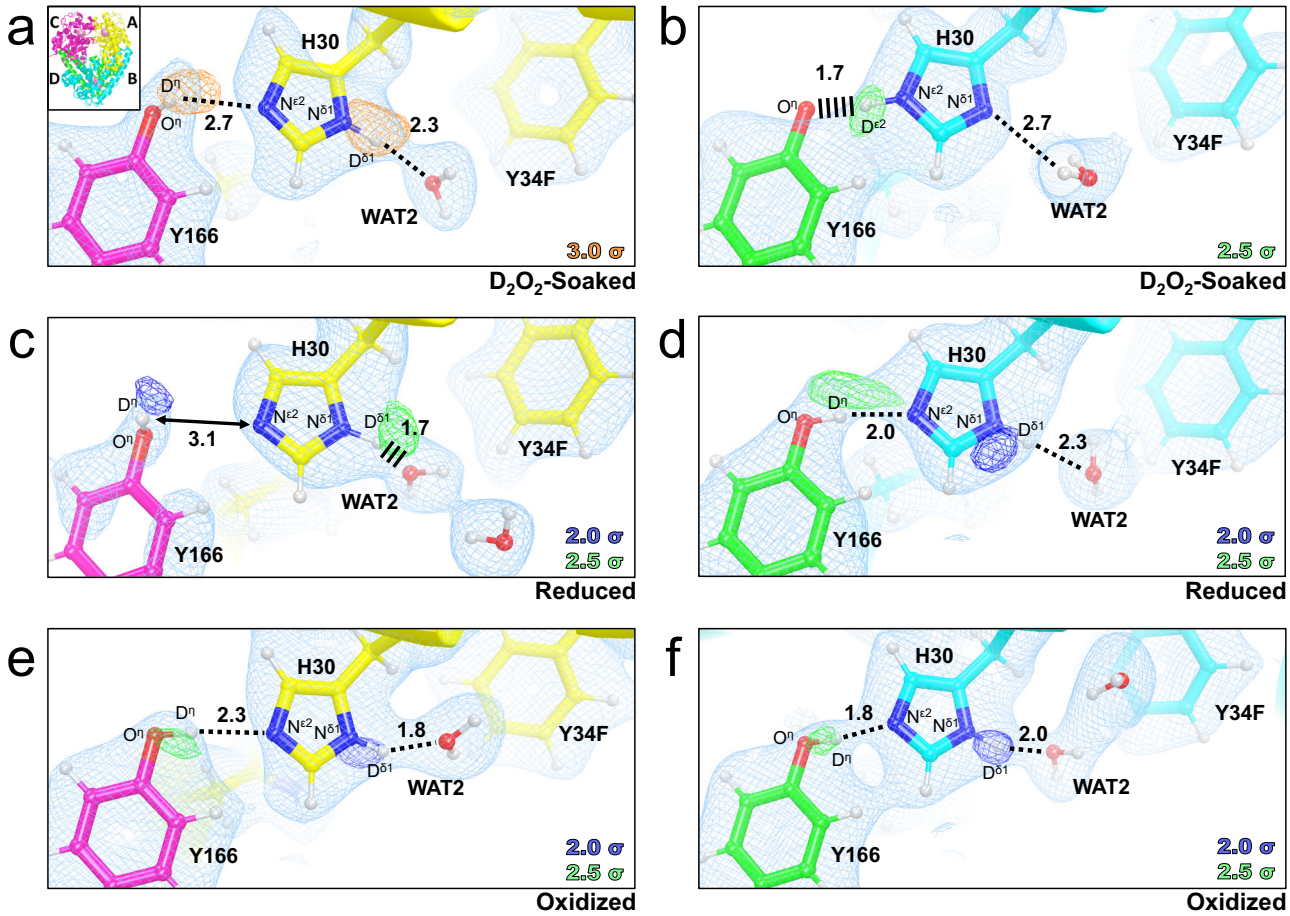

Fig. 4 | Protonation states of Tyr166 and His30 in Tyr34Phe MnSOD between adjacent subunits across the dimeric protein-protein interface. a, **b** Neutron structures of D_2O_2-soaked Tyr34Phe MnSOD (2.3 Å resolution). **c**, **d** Neutron structures of Tyr34Phe Mn^{2+}SOD (2.5 Å resolution). **e**, **f** Neutron structures of Tyr34Phe Mn^{3+}SOD (2.3 resolution). Blue, green, and orange omit $|F_o|$ - $|F_c|$ difference neutron scattering length density of protons displayed at 2.0 σ, 2.5σ, and 3.0σ, respectively. Light blue $2|F_o|$ - $|F_c|$ density is displayed at 1.0σ. Distances are in Å. Dashed lines indicate hydrogen bonds ≥ 1.8 Å and hashed lines indicate SSHBs that are hydrogen bonds < 1.8 Å. Chains are colored according to the inset in Fig. 4a.

comparisons show the importance of the WAT1-Gln143 interaction for catalysis and hydrogen bonding correlates with longer retention of the inhibited complex.

The electronic configuration of the Mn ion

For enzymes that use metal centers to catalyze redox reactions, the arrangement of the metal 3 d orbitals determines how electrons are exchanged and how substrates orient for catalysis[79]. A detailed analysis of the electronic configuration of the Mn ion is presented in the Supplementary information and is summarized here. For MnSOD, the metal ion is in a distorted C_{3v} symmetry environment with either 4 or 5 occupied electrons in the α-manifold, depending on the oxidation state of the metal[67]. For Mn^{3+} with S = 2, the e_π (xz/yz) and e_σ (xy/x^2-y^2) α orbitals are occupied, while Mn^{2+} with S = 5/2 also has the z^2 α orbital occupied (Supplementary Fig. 4a). The z^2 α orbital exchanges electrons during redox reactions as it is the lowest unoccupied molecular orbital (LUMO) for Mn^{3+} and the highest occupied molecular orbital (HOMO) for Mn^{2+}. This means that mono- or dioxygen species are most likely to bind the Mn ion along the z-axis for reactivity (Supplementary Fig. 4b). For further insight into the MnSOD metal 3 d orbitals, we compared the K-pre-edge spectra found through time-dependent DFT (TD-DFT) simulations with spectra measured from HERFD-XANES (detailed evaluation of these data can be found in the Supplementary Information pages 16-18 and Supplementary Table 5 and Fig. 4). We found that the experimental pre-edge spectra are similar between wildtype and Tyr34Phe Mn^{3+}SOD, indicating that the Tyr34Phe variant does not significantly alter the Mn^{3+} ion orbital configuration (Supplementary Figs. 4c, d). Also, the H_2O_2-soaked Trp161Phe and Tyr34Phe complexes have similar experimental spectra though the calculated spectra suggest differences in orbital transitions (Supplementary Figs. 4g, h).

Tyr34 contributes to the pK_as of Tyr166/His30 and influences the proton shuffle across the subunit interface

Second-sphere residues His30 and Tyr166 have unusual pK_as in wildtype MnSOD and change protonation states (Fig. 1c)[13]. To identify whether the Tyr34 mutation to Phe affects the protonations of His30/Tyr166, we investigated the nuclear density maps of Tyr34Phe MnSOD in D_2O_2-soaked, reduced, and oxidized forms. For chain A of D_2O_2-soaked MnSOD that has a dioxygen species bound (Fig. 3a, b), the omit $|F_o|$ - $|F_c|$ density indicates that Tyr166 is in the neutral, protonated form while His30 is singly protonated on the $N^{δ1}$ atom (Fig. 4a). Interestingly, for chain B, Tyr166 is instead deprotonated and His30 is now protonated on $N^{ε2}$ (Fig. 4b). The two residues form a 1.7 Å SSHB due to the negative charge of ionized Tyr166. Different chains of the same MnSOD neutron structure have been observed before to differ in protonation states, with the most explicable cause being differences in solvent accessibility[13]. However, the protonation configuration observed in chain B is unique and has not been seen before (Fig. 4b). It is not known if this proton configuration occurs in wildtype enzyme as

neutron data for D_2O_2-soaked wildtype has yet to be collected. But we can compare reduced and oxidized Tyr34Phe MnSOD to wildtype[13].

For reduced Tyr34Phe MnSOD, both chains have the same protonation states (Fig. 4c, d). Tyr166 is protonated and neutral while His30 is singly-protonated on the $N^{\delta1}$ atom. The omit density for D^{η}(Tyr166) is elongated and spans to $N^{\varepsilon2}$(His30) (Fig. 4d). Elongated density has been observed between the two residues before in reduced wildtype MnSOD[13]. This may be indicative of a proton transfer occurring between Tyr166 and His30, in line with the different protonation states observed in the D_2O_2-soaked structure (Fig. 4a, b).

The protonation states of oxidized Tyr34Phe (Fig. 4e, f) are the same as reduced Tyr34Phe (Fig. 4c, d), which is in contrast to wildtype MnSOD where the His30 protonation alters between oxidized and reduced states (Fig. 1c). This difference is probably due to the Phe mutation at position 34. In wildtype, Tyr34 is ionized when the Mn ion is oxidized (Fig. 1d). The negative charge on Tyr34 may exert electronic effects that alter the pK_a of His30. Thus, Tyr34 may help modulate the pK_a of nearby residues so efficient proton transfers occur for PCET catalysis.

Our three neutron structures of Tyr34Phe MnSOD highlight the importance of residues Tyr166, His30, and Tyr34 in maintaining the proton pool of the active site. Two protons are needed to protonate O_2^{2-} to H_2O_2 during the fast $Mn^{2+} \rightarrow Mn^{3+}$ reaction (k_2, Supplementary Table 1). The D_2O_2-soaked structure unambiguously indicates that His30 and Tyr166 shuffle protons, with proton transfers between O^{η}(Tyr166) and $N^{\varepsilon2}$(His30) coinciding with changes in the $N^{\delta1}$(His30) protonation state (Fig. 4a, d). In wildtype MnSOD, the proton between O^{η}(Tyr166) and $N^{\varepsilon2}$(His30) was instead observed to be shared, perhaps because the wildtype structures were collected at room temperature (Fig. 1c, d). Another distinction between Tyr34Phe and wildtype MnSOD is that in the oxidized forms, the $N^{\delta1}$(His30) have different protonation states. For Tyr34Phe, $N^{\delta1}$(His30) is protonated (Fig. 4e, f) while in wildtype $N^{\delta1}$(His30) is deprotonated (Fig. 1c). The pK_as of active site residues are a result of multiple effects, including residue composition and ionization states. An ionized Tyr34 coincides with a deprotonated $N^{\delta1}$(His30) in wildtype MnSOD and suggests that Tyr34 contributes to modulating the pK_a of nearby residues for oxidized MnSOD. Overall, the Tyr34Phe MnSOD neutron structures help elucidate the role of Tyr166, His30, and Tyr34 in MnSOD catalysis.

Summary and comparison of Tyr34Phe active site configurations

Comparing the Tyr34Phe MnSOD neutron structures with our previous wildtype and Trp161Phe neutron structures helps our understanding of the role of Tyr34 in catalysis. For oxidized wildtype and Tyr34Phe MnSOD, the WAT1-Gln143 protonation states and hydrogen bond interaction are similar (Fig. 5a, b). However, in reduced Tyr34Phe, His30 is observed to have different protonation states compared to wildtype, and the proton between His30 and Tyr166 is not shared. For the reduced counterparts, the hydrogen bonding of Gln143 with WAT1 and Trp123 is weaker in Tyr34Phe MnSOD (Fig. 5c, d). The Gln143 hydrogen bonds in wildtype are SSHBs (<1.8 Å), while those of Tyr34Phe are typical hydrogen bonds (>1.8 Å). Reduced wildtype is observed to have a shared proton between His30 and Tyr166 while Tyr34Phe does not. However, chain B of reduced Tyr34Phe MnSOD is observed to have elongated nuclear density between His30 and Tyr166 (Fig. 4d), which indicates that a proton may be shared. For peroxide-bound Trp161Phe and Tyr34Phe, HO_2^- binds the Mn ion in different orientations (Fig. 5e, f). Furthermore, in Trp161Phe, a H_2O_2 molecule is bound with SSHBs between His30 and an anionic Tyr34. The lack of H_2O_2 at this site in Tyr34Phe may be due to the absence of the hydroxyl group. Overall, Tyr34 plays a role in several aspects of the active site, and several enzymatic details are revealed from this collection of neutron structures.

First, Tyr34 helps control the charge at the active site and provides an environment conducive to charge-dependent proton and electron transfers. For example, Tyr34 and His30 both lose protons when the active site is oxidized and gain protons when the active site is reduced (Figs. 5a, 5c, 1c, d). As a result, we previously hypothesized that Tyr34 and His30 protonate O_2^{2-} during the fast $Mn^{2+} \rightarrow Mn^{3+}$ reaction (k_2, Supplementary Table 1)[13]. In the Tyr34Phe variant, the His30 protonation state remains consistent between resting states, which implicates Tyr34 in influencing the pK_a of His30 through electronic effects (Figs. 5b, d, 4c-f). These charge effects of Tyr34 may be a partial contributor to the deficient catalysis observed for the Tyr34Phe variant (Supplementary Table 1).

Second, Tyr34 plays a significant role in the fast $Mn^{2+} \rightarrow Mn^{3+}$ reaction as suggested by the very low k_2 for Tyr34Phe (Supplementary Table 1). Comparison of the resting Mn^{2+}SOD neutron structures of wildtype and Tyr34Phe indicates that Tyr34 enforces a strong WAT1-Gln143 interaction (Figs. 5c, d, 3d). This interaction is important for PCET, where the WAT1 → Gln143 proton transfer coincides with the $Mn^{2+} \rightarrow Mn^{3+}$ redox reaction (Fig. 1b)[13]. Another potential reason for diminished k_2 catalysis for the Tyr34Phe variant is the loss of an ionizable group that could protonate O_2^{2-} or HO_2^-. However, the Trp161Phe variant also has a nearly extinguished k_2 and maintains the number of ionizable groups (Supplementary Table 1). The shared feature for these two variants is the weakened WAT1-Gln143 interaction (Fig. 4f). Since our previous structures indicate that Tyr34 loses a proton during the $Mn^{2+} \rightarrow Mn^{3+}$ reaction (Fig. 1d), it is possible that the WAT1 → Gln143 proton transfer precludes a Tyr34 → O_2^{2-} proton transfer. Overall, our structures indicate Tyr34 contributes to orienting WAT1 and Gln143 for a proton transfer event during the $Mn^{2+} \rightarrow Mn^{3+}$ redox reaction.

Third, the formation of the product-inhibited complex is dependent on Tyr34. The complex is characterized by an HO_2^- molecule replacing the WAT1 position in the Mn^{2+} oxidation state (Fig. 5e, f, Supplementary Fig. 3e). As such, the capacity to form the inhibited complex may correlate with the ease an HO_2^- molecule can displace WAT1. The Tyr34Phe and Trp161Phe variants have a higher propensity to accumulate the inhibited complex, and both have a weakened WAT1-Gln143 interaction in the Mn^{2+} oxidation state that would permit easier displacement of WAT1 (Fig. 4f). This suggests that the Tyr34-Gln143-WAT1 hydrogen bond network suppresses product inhibition.

Lastly, retention of the product-inhibited complex correlates with the strength of hydrogen bonding between HO_2^- and Gln143. The inhibited complexes captured in the Tyr34Phe and Trp161Phe variants reveal two different HO_2^- binding orientations and hydrogen bond interactions (Fig. 5e, f, Supplementary Fig. 3e). The hydrogen bonding between HO_2^- and Gln143 is stronger in Trp161Phe compared to Tyr34Phe, and this stronger interaction correlates with a slower dissociation of the inhibited complex for Trp161Phe (k_4, Supplementary Table 1). As protonation of HO_2^- to H_2O_2 is required for relief of the inhibited complex, the hydrogen bonding of Gln143 with HO_2^- may compete with a $H_2O \rightarrow HO_2^-$ proton transfer to form H_2O_2. Comparison of the product-inhibited complex of Tyr34Phe and Trp161Phe provides clues into the relief of the inhibited complex.

Suggested mechanism

From our collection of neutron structures and XAS data, we have constructed a mechanism for the fast reaction pathways k_1 and k_2 and the reversible product inhibition reaction pathways k_3 and k_4 (Fig. 6). Note that our data describe the inhibited complex as Mn^{2+}-containing (Figs. 2a, Supplementary Fig.3a–c), in contrast with several mechanistic models that assign a Mn^{3+} oxidation state to the complex[31–33,59,60]. Furthermore, in the absence of data that describe how $O_2^{\bullet-}$ interacts with an oxidized active site, $O_2^{\bullet-}$ reacting with the Mn^{3+} ion is represented only by Mn^{3+} gaining an electron (Fig. 6). For a reduced active site, $O_2^{\bullet-}$ likely binds between His30 and Tyr34 for PCET to form

https://doi.org/10.1038/s41467-025-57180-3

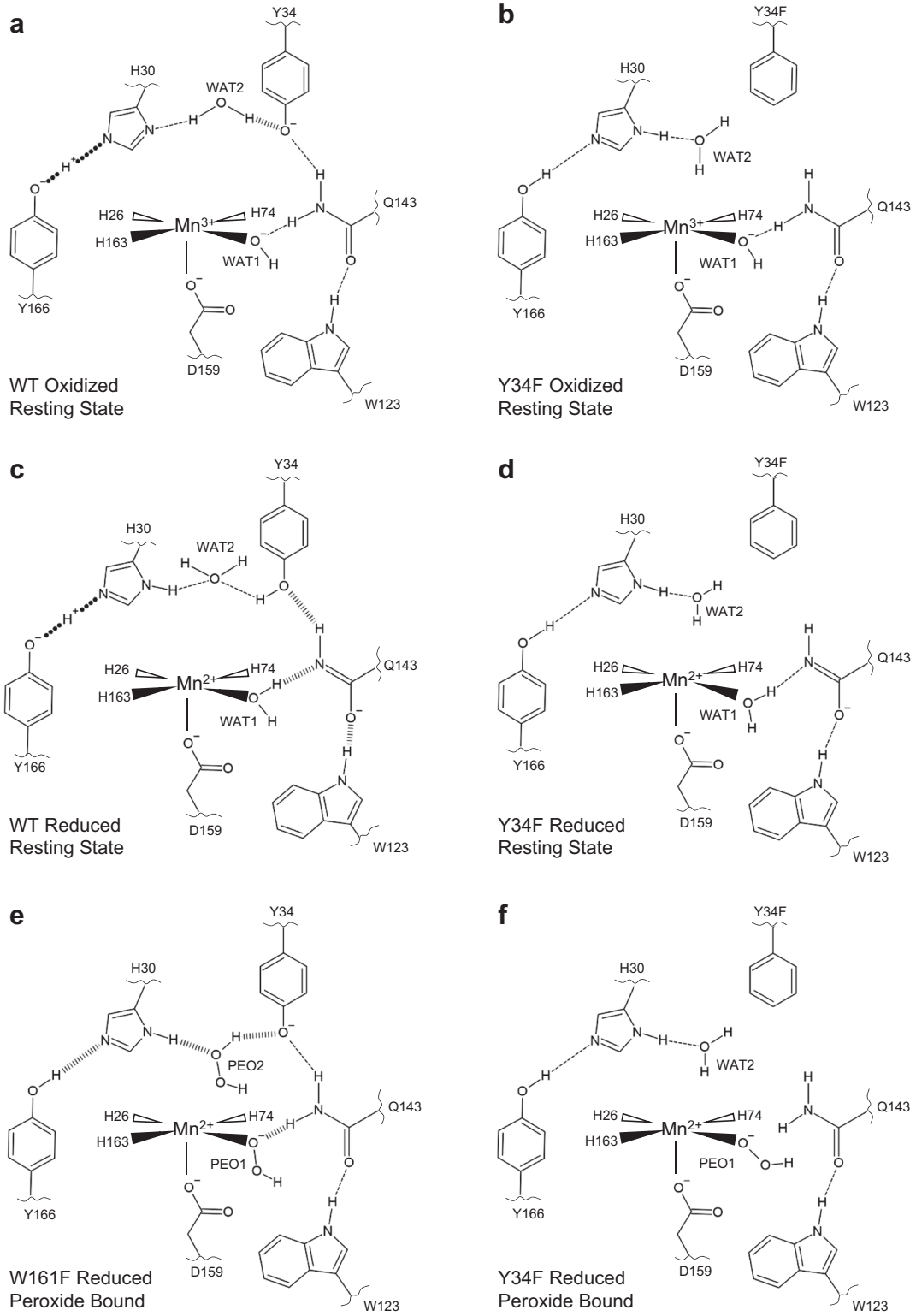

Fig. 5 | Comparison of Tyr34Phe MnSOD active site configurations to wildtype and Trp161Phe. a Wildtype oxidized resting state from chain B of PDB ID 7KKS[13]. **b** Tyr34Phe oxidized resting state from chain A (present study, Figs. 3e, 4e). **c** Wildtype reduced resting state from chain B of PDB ID 7KKW[13]. **d** Tyr34Phe reduced resting state from chain A (present study, Figs. 3c, 4c). **e** The product-inhibited complex of Trp161Phe, consisting of a HO_2^- molecule bound to a reduced active site. From chain B of PDB ID 8VHW[63]. **f** The product-inhibited complex of Tyr34Phe, consisting of a HO_2^- molecule bound to a reduced active site. From chain A of the present study (Figs. 3a, b, 4a). Dashed lines represent normal hydrogen bonds (> 1.8 Å), wide-dashed represent SSHBs (hydrogen bonds < 1.8 Å), and round-dotted lines represent a shared proton. The portrayal of hydrogen bond lengths in 2D are not representative of those seen experimentally in 3D.

https://doi.org/10.1038/s41467-025-57180-3

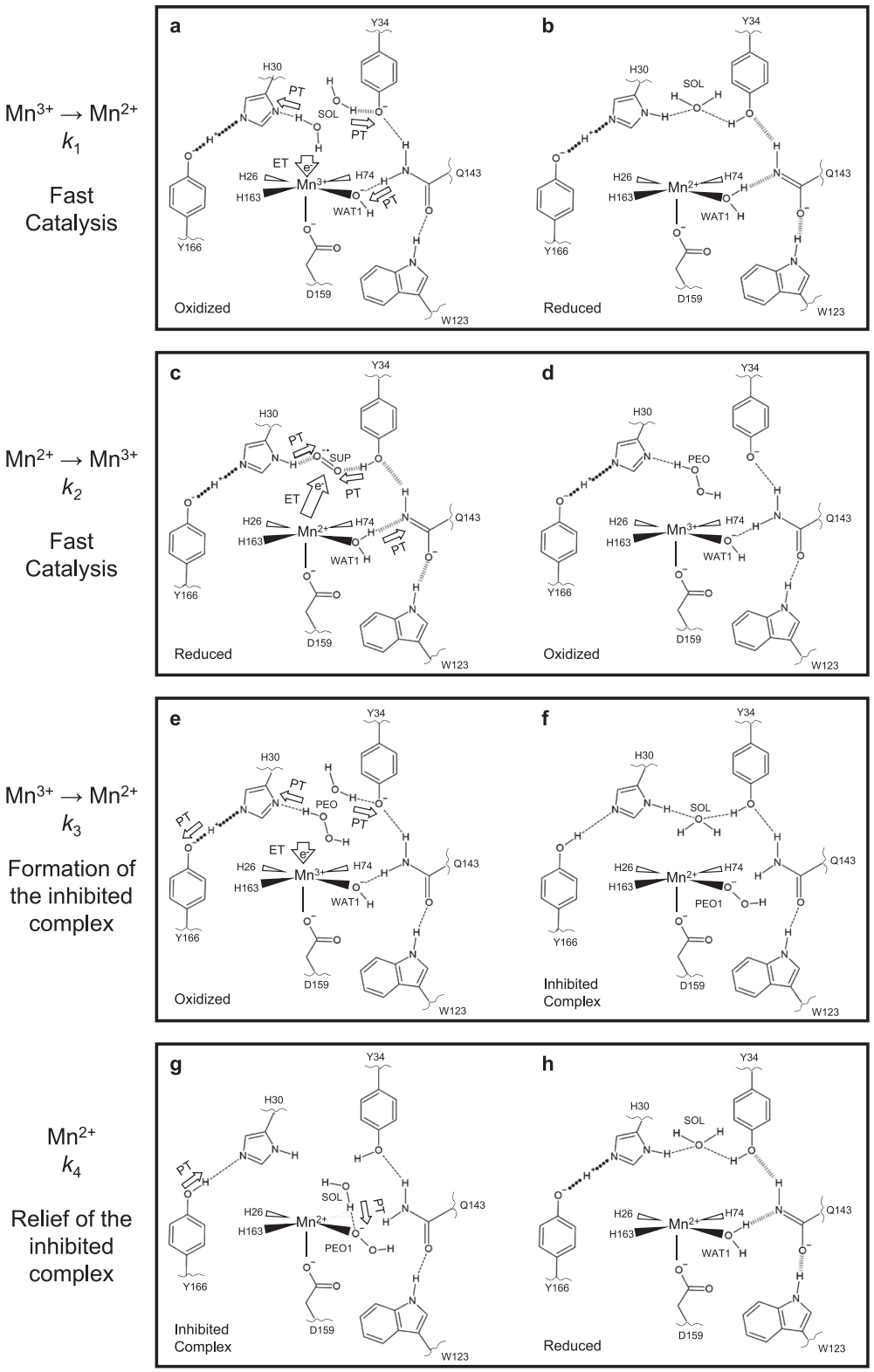

H_2O_2[13,41]. Overall, the mechanism delineates how MnSOD's reversible inhibition pathway may branch from the fast reaction pathway.

For the k_1 reaction that represents the fast $Mn^{3+} \rightarrow Mn^{2+}$ half-reaction, reduction of the Mn ion occurs alongside three proton transfers, Gln143 → WAT1 and protonation of His30 and Tyr34 by solvent (Fig. 6a). In the reduced state, anionic Gln143 is stabilized by SSHBs with Trp123, WAT1, and Tyr34 (Fig. 6b). For the k_2 reaction that represents the fast $Mn^{2+} \rightarrow Mn^{3+}$ half-reaction, a WAT1 → Gln143 proton transfer occurs alongside protonation and reduction of $O_2^{\bullet-}$ (Fig. 6c). Here, $O_2^{\bullet-}$ participates in a long-range electron transfer and is protonated by His30 and Tyr34 to form H_2O_2 (Fig. 6d). If Mn^{3+} gains an electron while the resultant H_2O_2 is still present, H_2O_2 donates a proton to His30 and subsequently replaces WAT1 to form the product inhibited complex (k_3, Fig. 6e, f). The inhibited complex is characterized by

Fig. 6 | Suggested reaction mechanism of MnSOD. The associating and dissociating molecules are indicated by the reaction on the left side of the figure for each panel. **a**, **b** The fast $Mn^{3+} \rightarrow Mn^{2+}$ half-reaction corresponding to k_1. Note that the electrons are contributed to by superoxide binding. The location of this binding site is still unknown, so this is indicated with a thick arrow. **c**, **d** The fast $Mn^{2+} \rightarrow Mn^{3+}$ half-reaction corresponding to k_2. **e**, **f** Formation of the inhibited complex that is dependent on the presence of H_2O_2 during the reduction of the Mn^{3+} ion. In the absence of H_2O_2, the enzyme proceeds through the fast $Mn^{3+} \rightarrow Mn^{2+}$ half-reaction (k_1). **g**, **h** Relief of the inhibited complex. Our data describe the inhibited complex as Mn^{2+}-containing in contrast to other published mechanistic models[31–33,59,60]. In the absence of data that indicate how $O_2^{\bullet-}$ interacts with an oxidized active site, $O_2^{\bullet-}$ reacting with the Mn^{3+} ion is represented only by Mn^{3+} gaining an electron. For a reduced active site, $O_2^{\bullet-}$ likely binds between His30 and Tyr34 for PCET to form H_2O_2[13,41]. Dashed lines represent normal hydrogen bonds (>1.8 Å), wide-dashed represent SSHBs (hydrogen bonds < 1.8 Å), and round-dotted lines represent a shared proton. The portrayal of hydrogen bond lengths in 2D are not representative of those seen experimentally in 3D.

the inability to perform the WAT1 → Gln143 proton transfer and prohibits fast catalysis (Fig. 6f). Relief of the inhibited complex is achieved by protonation of HO_2^- by a solvent molecule (k_4, Fig. 6g). H_2O_2 departs the active site and is replaced by WAT1 to form the Mn^{2+} resting state (Fig. 6h). From relief of inhibition, fast catalysis may proceed again through k_2 (Fig. 6c, d).

The key determinant of whether product inhibition is engaged is the His30 proton donor during Mn^{3+} reduction. If H_2O_2 is the proton donor, the inhibited complex is formed (k_3, Fig. 6e). If a solvent molecule is the proton donor, the enzyme proceeds through fast catalysis (k_1, Fig. 6a). This explains why high concentrations of $O_2^{\bullet-}$ lead to product inhibition, as $O_2^{\bullet-}$ may enter the active site before H_2O_2 departs. Tyr34 may also serve as a potential proton acceptor for H_2O_2 since Tyr34 also gains a proton during reduction to Mn^{2+}. However, Tyr34 is not necessary to form the inhibited complex, as indicated by our Tyr34Phe neutron structure (Fig. 3a, b). Our work provides insights into the PCET mechanism of MnSOD, especially in the context of product inhibition.

Altogether, our investigation reveals how a single tyrosine residue has a profound effect on PCET catalysis. Tyr34 plays a part in every MnSOD kinetic step from its roles of (1) acting as a proton donor/acceptor, (2) orienting nearby molecules Gln143 and WAT1 for proton transfer, (3) limiting the formation of the inhibited complex, and (4) shortening the lifetime of the inhibited complex. These roles of Tyr34 place the residue as a central regulator of H_2O_2 output in the mitochondria. H_2O_2 produced from MnSOD has several cellular effects, including stimulating apoptotic signaling pathways[45,46], coordinating protein localization and activity[47], and mitochondrial biogenesis[44]. Inactivation of Tyr34 by nitration is observed in neurological disease and further highlights the physiological role of Tyr34[58]. In total, the work provides insight into how a PCET enzyme facilitates catalysis and how an oxidoreductase molecularly facilitates mitochondrial function.

Methods

Perdeuterated expression and purification

For deuterated protein expression of MnSOD, the pCOLADuet-1 expression vector harboring full-length cDNA of *MnSOD* was transformed into *Escherichia coli* BL21(DE3) cells. Transformed cells were grown in D_2O minimal media within a bioreactor vessel using D_8-glycerol as the carbon source[80]. Induction was performed with 1 mM isopropyl β-D-thiogalactopyranoside, 8 mM $MnCl_2$, and fed D_8-glycerol until an OD_{600} of 15.0. Expression was performed at 37 °C for optimal Mn metal incorporation[81]. Harvested cell pastes were stored at -80 °C until purification. For protein purification (with hydrogenated reagents), cells were resuspended in a solution of 5 mM $MnCl_2$ and 5 mM 3-(*N*-morpholino)propanesulfonic acid (MOPS), pH 7.8. Clarified lysate was incubated at 55 °C to precipitate contaminant proteins that were subsequently removed by centrifugation. Next, soluble protein was diluted with an equal volume of 50 mM 2-(*N*-morpholino)ethanesulfonic acid (MES) pH 5.5, yielding a final concentration of 25 mM. Measurement of pH verified a value of 5.5 after dilution. Protein was applied onto a carboxymethyl sepharose fast flow column (GE Healthcare) and eluted with a sodium chloride gradient that contained 50 mM MES pH 6.5.

Crystallization

Perdeuterated Tyr34Phe MnSOD crystals were grown in a microgravity environment aboard the International Space Station (ISS)[82]. Crystals growth was achieved in Granada Crystallization Boxes (GCBs, Triana) through capillary counterdiffusion using fused quartz capillary tubes (VitroCom) that had inner diameters of 2.0 mm and outer diameters of 2.4 mm[83]. 25 mg ml^{-1} protein-filled capillaries were plugged with 40 mm of 2% agarose (*w*/*w*) and inserted into GCBs filled with precipitating agent composed of 4 M potassium phosphate, pH 7.8. The pH of the phosphate buffer was achieved through 91:9 ratios of K_2HPO_4:KH_2PO_4. The GCBs were delivered to the ISS by SpX-17 as part of the *Perfect Crystals* NASA payload and returned to earth 1 month later on SpX-18. The crystals within GCBs were observed to be resilient against travel damage and were placed within carry-on baggage during further aircraft travels to the UNMC Structural Biology Core Facility and ORNL. Perdeuterated Tyr34Phe MnSOD crystals were 0.3-0.6 mm^3 in size, and further details of microgravity crystallization have been published[82]. For X-ray diffraction, crystals were grown in 1.8 M potassium phosphate, pH 7.8 by hanging-drop vapor diffusion. Protein (23 mg ml^{-1}) and reservoir solution were mixed at a 1:1 ratio to give a 4.0 μL drop. Crystals for X-ray diffraction were less than 0.1 mm^3 in size and were fully grown after 14 d.

Crystal manipulations

For deuterium exchange, microgravity-grown crystals were first placed in 1 mL of hydrogenated 4 M potassium phosphate pH 7.8. Deuterium was introduced with 0.1 mL incremental additions every 2 min of 4 M deuterated potassium phosphate (K_2DPO_4:KD_2PO_4) pD 7.8 (calculated by adding 0.4 to the measured pH reading) for a total of five times and a net volume addition of 0.5 mL. After 10 min, 0.5 mL of the solution was removed leading to a 1 mL solution consisting of 33% deuterium. The process was repeated enough times to gradually increase the deuterium content to ~100%. The 4 M deuterated potassium phosphate also served as the cryoprotectant for the cryocooling process. Further details of the process were published[84].

For redox manipulation, the deuterated potassium phosphate solutions were supplemented with either 6.4 mM potassium permanganate ($KMnO_4$) to achieve the Mn^{3+} oxidation state or 300 mM sodium dithionite ($Na_2S_2O_4$) to achieve the Mn^{2+} state. Crystals were either sealed in capillaries or 9-well glass plates to maintain the desired oxidation state. Redox reagents were not used for the Tyr34Phe MnSOD structure soaked with D_2O_2. The crystal was in the as is resting state, which is >90% oxidized. The dioxygen-bound complex was achieved by supplementing the cryoprotectant that the crystal was immersed in with D_2O_2 at a final concentration of 1% *w*/*v* (~0.28 M) and soaking for 1 min before cryocooling. Flash-cooling was performed with an Oxford diffraction cryostream[85]. Further details of ligand cryotrapping for neutron crystallography were published[84].

Crystallographic data collection

Time-of-flight, wavelength-resolved neutron Laue diffraction data were collected from perdeuterated crystals using the MaNDi instrument[86,87] at the Oak Ridge National Laboratory Spallation Neutron Source with wavelengths between 2 to 4 Å. Sample sizes ranged from 0.3 to 0.6 mm^3 and data were collected to 2.30 Å resolution for

oxidized and D_2O_2-soaked structures, while the reduced structure was collected to 2.5 Å resolution (Supplementary Table 6). Crystals were held in stationary positions during diffraction, and successive diffraction frames were collected along rotations of the Φ axis. X-ray diffraction data were collected using a Rigaku FR-E SuperBright home source or the Stanford Synchrotron Radiation Lightsource (SSRL) beamline 14–1 (Supplementary Table 6).

Crystallographic data processing and refinement

Neutron data were integrated using the MANTID software package[88–90] and wavelength-normalized and scaled with LAUENORM from the Daresbury Laue Software Suite[91]. X-ray diffraction data were processed using HKL-3000[92]. Refinements of both neutron and X-ray models were completed separately with PHENIX.REFINE from the PHENIX suite[93]. The refinements were intentionally performed separately due to the known perturbations that X-rays have on the solvent structure, metal redox state, and metal coordination[34,94]. The X-ray model was first refined against its corresponding data set and subsequently used as the starting model for neutron refinement. Torsional backbone angle restraints were derived from the X-ray model and applied to neutron refinement using a geometric target function with PHENIX.REFINE[93]. Mn-ligand restraints for neutron refinement were derived from DFT calculations rather than the X-ray model to remove any influence of photoreduction. The neutron refinement was performed by modeling the D atoms of the active site last to limit phase bias. Initial rounds of refinement to fit protein structure included only non-exchangeable D atoms, which have stereochemical predictable positions. Afterward, H/D atoms were modeled onto the position of each amide proton, and occupancy was refined. In general, the asymmetric units of the neutron crystal structures had a deuterium content of ~85% for the amide backbone, and areas with low deuterium exchange (<50 %) coincided with the presence of hydrogen bonds forming a secondary structure. Next, exchangeable proton positions of residues outside the active site (e.g., hydroxyl group of serine/tyrosine) were manually inspected for obvious positive omit $|F_o| - |F_c|$ neutron scattering length density at a contour of 2.5σ or greater and modeled as a fully occupied deuterium. If the density was not obvious, and there was no chemically sensible reason for the residue to be deprotonated (which is the case for residues outside the active site), the proton position was H/D occupancy refined. D_2O molecules outside the active site were then modeled and adjusted according to the nuclear density. Last, D atoms of the active site were modeled manually. At the active site, a residue is considered deprotonated when (1) attempts to model and refine a proton result in negative $|F_o| - |F_c|$ difference neutron scattering length density, (2) all the other protons of the residue can be placed, and (3) the heavy atom that is deprotonated acts as a hydrogen-bond acceptor. As chemically ideal covalent bond distances of D atoms were ensured during model building and refinement, small deviations from D atom positions and omit $|F_o| - |F_c|$ neutron scattering length density centers were expected from the data resolution (2.3–2.5 Å). To test if the active site ligands for chain A and chain B were truly different we performed a refinement forcing chain B to be identical to chain A. This resulted in difference density that supported our original structural interpretation of the D_2O_2-soaked structure (Supplementary Figs. 1a and 1b). Chain B is different than chain A as shown.

X-ray absorption spectroscopy measurements

A solution of 3 mM MnSOD (~70 mg ml^{-1}) in 25 mM potassium phosphate pH 7.8 was treated with 8 mM potassium dichromate to isolate the Mn^{3+}SOD resting state, 200 mM sodium dithionite to isolate the Mn^{2+}SOD resting state, and either 20 mM superoxide or 280 mM (1% *w/v*) hydrogen peroxide for the product-inhibited state. For EXAFS spectra the sample included 30% ethylene glycol to avoid water crystals. Samples were mounted in 150 μl mylar cells. Superoxide stock solutions were generated by mixing 1.3 M potassium superoxide (KO_2, Sigma Aldridge) in a mixture of dry DMSO (Thermo Scientific) and 0.30 M di-benzo-18-crown-6-ether (Thermo Scientific) following published protocols[59,60,62,95,96]. The concentration of superoxide in the DMSO/18-crown solution was measured by a UV-Vis spectrophotometer at a wavelength of 250 nm with a molar extinction coefficient of 2686 M^{-1} cm^{-1} [62,97]. Superoxide solutions were stored at 4 °C under a layer of argon in glass vials sealed with rubber septum.

Mn K-edge HERFD-XANES spectra were recorded at beamline 15-2 of the Stanford Synchrotron Radiation Lightsource (SSRL), while Mn K-edge EXAFS spectra were collected at beamline 7-3. At both beamlines, data were collected at 10 K using a liquid He cryostat, and the incident energy was tuned to the first derivative of an internal Mn foil at 6539 eV. X-ray irradiation was carefully monitored so that two subsequent scans of the same spot did not have photoreduction differences, and different spots along samples were scanned. When appropriate, aluminum foil was inserted into the beam path to attenuate the incident flux. For HERFD-XANES measurements, a Johann-type hard X-ray spectrometer with six Ge(333) analyzer crystals was used with a liquid-nitrogen cooled Si(311) double crystal monochromator, and energy was calibrated to a glitch with measurement of Mn Foil. For EXAFS, measurements were recorded with a 30-element Ge solid-state detector, and a Si(220) monochromator at Φ = 90° was used.

X-ray absorption spectroscopy data analysis

EXAFS data reduction, averaging, and refinement were carried out with the LARCH software package[98]. Refinement of the $k^2\chi(k)$ EXAFS data used phases and amplitudes obtained from, FEFF[99]. For each fit, optimization of the radial distribution around the absorbing Mn ion (r) and the Debye-Waller factor (σ^2) was performed. The goodness-of-it was evaluated by χ^2 values, reduced χ^2 values and R-factors.

Computational methods

All DFT calculations were performed with the ORCA quantum chemistry package version 5.0 using the B3LYP functional, the def2-TZVP basis set for all atoms, and the CPCM solvation model[100–103]. For geometry optimizations, the full active site (i.e., residues shown in the right panel of Fig. 1a) was included from the neutron structure where the peptide backbone was truncated and C^α was fixed. All atoms for residues Trp161, Phe66, and Tyr166 were fixed with the exception of hydroxyl Tyr166 proton to mimic the packing found in the native enzyme. The Mn ion used the high-spin quintet and sextet states for trivalent and divalent systems, respectively, per experimental observations[67]. A dense integration grid and tight convergence were enforced. For CPCM calculations, the dielectric constant was 80.4. The atomic radii were 2.04 Å for carbon, 1.86 Å for nitrogen, 1.32 Å for hydrogen, 1.82 Å for oxygen, and 2.40 Å for manganese. The solvent probe radius was 1.3 Å.

For TD-DFT calculations, the Mn ion was instead assigned the core property basis set, CP(PPP)[104,105]. The geometry-optimized model was truncated to only the Mn ion and its immediate ligands. Including all active site residues for TD-DFT did not significantly alter the simulated spectra. Computed Mn K pre-edge data were plotted using a Gaussian broadening of 1 eV, and a 32.3 eV energy correction was applied in line with previous studies[64,106].

Reporting summary

Further information on research design is available in the Nature Portfolio Reporting Summary linked to this article.

Data availability

Coordinates and structure factors for neutron and X-ray crystallographic data presented in this study have been deposited in the Protein Data Bank. (PDB 9BVY, PDB 9BW2, PDB 9BWM, PDB 9BWQ,

and PDB 9BWR. All relevant data supporting the key findings of this study are available within the article, its Supplementary Information files and in the Source Data file or from the corresponding author upon request. Source data are provided with this paper.

References

1. McDonald, A. G., Boyce, S. & Tipton, K. F. ExplorEnz: the primary source of the IUBMB enzyme list. *Nucleic Acids Res* **37**, D593–D597 (2009).
2. Costentin, C., Robert, M. & Saveant, J. M. Concerted proton-electron transfers: electrochemical and related approaches. *Acc. Chem. Res*. **43**, 1019–1029 (2010).
3. Chang, C. J., Chang, M. C., Damrauer, N. H. & Nocera, D. G. Proton-coupled electron transfer: a unifying mechanism for biological charge transport, amino acid radical initiation and propagation, and bond making/breaking reactions of water and oxygen. *Biochim Biophys. Acta* **1655**, 13–28 (2004).
4. Albers, D. S. & Beal, M. F. Mitochondrial dysfunction and oxidative stress in aging and neurodegenerative disease. *J. Neural Transm. Suppl.* **59**, 133–154 (2000).
5. Gao, L., Laude, K. & Cai, H. Mitochondrial pathophysiology, reactive oxygen species, and cardiovascular diseases. *Vet. Clin. North Am. Small Anim. Pr.* **38**, 137–155 (2008).
6. Lipinski, B. Hydroxyl radical and its scavengers in health and disease. *Oxid. Med Cell Longev.* **2011**, 809696 (2011).
7. Reece, S. Y. & Seyedsayamdost, M. R. Long-range proton-coupled electron transfer in the Escherichia coli class Ia ribonucleotide reductase. *Essays Biochem* **61**, 281–292 (2017).
8. Bhat, A. H. et al. Oxidative stress, mitochondrial dysfunction and neurodegenerative diseases; a mechanistic insight. *Biomed. Pharmacother.* **74**, 101–110 (2015).
9. Nielsen, J. E. & McCammon, J. A. Calculating pKa values in enzyme active sites. *Protein Sci.* **12**, 1894–1901 (2003).
10. Maliekal, J. et al. Comparison and contrasts between the active site PKs of Mn-superoxide dismutase and those of Fe-superoxide dismutase. *J. Am. Chem. Soc.* **124**, 15064–15075 (2002).
11. Pannwitz, A. & Wenger, O. S. Proton-coupled multi-electron transfer and its relevance for artificial photosynthesis and photoredox catalysis. *Chem. Commun. (Camb.)* **55**, 4004–4014 (2019).
12. Bhowmick, A. et al. Structural evidence for intermediates during O(2) formation in photosystem II. *Nature* **617**, 629–636 (2023).
13. Azadmanesh, J., Lutz, W. E., Coates, L., Weiss, K. L. & Borgstahl, G. E. O. Direct detection of coupled proton and electron transfers in human manganese superoxide dismutase. *Nat. Commun.* **12**, 2079 (2021).
14. Shrishrimal, S., Kosmacek, E. A., Chatterjee, A., Tyson, M. J. & Oberley-Deegan, R. E. The SOD Mimic, MnTE-2-PyP, Protects from Chronic Fibrosis and Inflammation in Irradiated Normal Pelvic Tissues. *Antioxid. (Basel)* **6**, 87 (2017).
15. Mapuskar, K. A. et al. Utilizing superoxide dismutase mimetics to enhance radiation therapy response while protecting normal tissues. *Semin Radiat. Oncol.* **29**, 72–80 (2019).
16. Batinic-Haberle, I. & Spasojevic, I. Complex chemistry and biology of redox-active compounds, commonly known as SOD mimics, affect their therapeutic effects. *Antioxid. Redox Signal* **20**, 2323–2325 (2014).
17. Stover, K. et al. Topically applied manganese-porphyrins BMX-001 and BMX-010 display a significant anti-inflammatory response in a mouse model of allergic dermatitis. *Arch. Dermatol Res.* **308**, 711–721 (2016).
18. You, C., Huang, R., Wei, X., Zhu, Z. & Zhang, Y. P. Protein engineering of oxidoreductases utilizing nicotinamide-based coenzymes, with applications in synthetic biology. *Synth. Syst. Biotechnol.* **2**, 208–218 (2017).
19. Shields, H. J., Traa, A. & Van Raamsdonk, J. M. Beneficial and detrimental effects of reactive oxygen species on lifespan: a comprehensive review of comparative and experimental studies front. *Cell Dev. Biol.* **9**, 628157 (2021).
20. Wallace, D. C. Mitochondria and cancer. *Nat. Rev. Cancer* **12**, 685–698 (2012).
21. De Gaetano, A. et al. *Mitophagy and Oxidative Stress: The Role of Aging Antioxidants (Basel)*, **10** (2021).
22. Fukai, T. & Ushio-Fukai, M. Superoxide dismutases: role in redox signaling, vascular function, and diseases. *Antioxid. Redox Signal* **15**, 1583–1606 (2011).
23. Pinero, J. et al. The DisGeNET knowledge platform for disease genomics: 2019 update. *Nucleic Acids Res* **48**, D845–D855 (2020).
24. Li, C. & Zhou, H. M. The role of manganese superoxide dismutase in inflammation defense. *Enzym. Res.* **2011**, 387176 (2011).
25. Nowak-Kiczmer, M., Niedziela, N., Zalejska-Fiolka, J. & Adamczyk-Sowa, M. Evaluation of antioxidant parameters of multiple sclerosis patients' serum according to the disease course. *Mult. Scler. Relat. Disord.* **77**, 104875 (2023).
26. Souiden, Y. et al. MnSOD and GPx1 polymorphism relationship with coronary heart disease risk and severity. *Biol. Res* **49**, 22 (2016).
27. Perry, J. J., Shin, D. S., Getzoff, E. D. & Tainer, J. A. The structural biochemistry of the superoxide dismutases. *Biochim Biophys. Acta* **1804**, 245–262 (2010).
28. Azadmanesh, J. & Borgstahl, G. E. O. A Review of the Catalytic Mechanism of Human Manganese Superoxide Dismutase. *Antioxid. (Basel)* **7**, 25 (2018).
29. Cadenas, E. & Davies, K. J. Mitochondrial free radical generation, oxidative stress, and aging. *Free Radic. Biol. Med* **29**, 222–230 (2000).
30. Drose, S. & Brandt, U. The mechanism of mitochondrial superoxide production by the cytochrome bc1 complex. *J. Biol. Chem.* **283**, 21649–21654 (2008).
31. Abreu, I. A. & Cabelli, D. E. Superoxide dismutases-a review of the metal-associated mechanistic variations. *Biochim Biophys. Acta* **1804**, 263–274 (2010).
32. Sheng, Y. et al. Superoxide dismutases and superoxide reductases. *Chem. Rev.* **114**, 3854–3918 (2014).
33. Hearn, A. S. et al. Kinetic analysis of product inhibition in human manganese superoxide dismutase. *Biochemistry* **40**, 12051–12058 (2001).
34. O'Dell, W. B., Bodenheimer, A. M. & Meilleur, F. Neutron protein crystallography: A complementary tool for locating hydrogens in proteins. *Arch. Biochem Biophys.* **602**, 48–60 (2016).
35. Carugo, O. & Djinovic Carugo, K. When X-rays modify the protein structure: radiation damage at work. *Trends Biochem Sci.* **30**, 213–219 (2005).
36. Remer, L. C. & Jensen, J. H. Toward a general theory of hydrogen bonding: the short, strong hydrogen bond. *J. Phys. Chem. A* **104**, 9266–9275 (2000).
37. Gerlt, J. A., Kreevoy, M. M., Cleland, W. & Frey, P. A. Understanding enzymic catalysis: the importance of short, strong hydrogen bonds. *Chem. Biol.* **4**, 259–267 (1997).
38. Kumar, P., Agarwal, P. K. & Cuneo, M. J. On the case of the misplaced hydrogens. *Chembiochem.* **22**, 288–297 (2020).
39. Cleland, W. W., Frey, P. A. & Gerlt, J. A. The low barrier hydrogen bond in enzymatic catalysis. *J. Biol. Chem.* **273**, 25529–25532 (1998).
40. MacMillan-Crow, L. A. & Thompson, J. A. Tyrosine modifications and inactivation of active site manganese superoxide dismutase mutant (Y34F) by peroxynitrite. *Arch. Biochem Biophys.* **366**, 82–88 (1999).
41. Srnec, M., Aquilante, F., Ryde, U. & Rulisek, L. Reaction mechanism of manganese superoxide dismutase studied by combined

quantum and molecular mechanical calculations and multi-configurational methods *J. Phys. Chem. B*,**113**, 6074–6086 (2009).
42. Lah, M. S. et al. Structure-function in Escherichia coli iron superoxide dismutase: comparisons with the manganese enzyme from Thermus thermophilus. *Biochemistry* **34**, 1646–1660 (1995).
43. Whittaker, M. M. & Whittaker, J. W. Low-temperature thermochromism marks a change in coordination for the metal ion in manganese superoxide dismutase. *Biochemistry* **35**, 6762–6770 (1996).
44. Palma, F. R. et al. Mitochondrial superoxide dismutase: what the established, the intriguing, and the novel reveal about a key cellular redox switch. *Antioxid. Redox Signal* **32**, 701–714 (2020).
45. Dasgupta, J. et al. Manganese superoxide dismutase protects from TNF-alpha-induced apoptosis by increasing the steady-state production of H2O2. *Antioxid. Redox Signal* **8**, 1295–1305 (2006).
46. Cadenas, E. Mitochondrial free radical production and cell signaling. *Mol. Asp. Med.* **25**, 17–26 (2004).
47. Riemer, J., Schwarzlander, M., Conrad, M. & Herrmann, J. M. Thiol switches in mitochondria: operation and physiological relevance. *Biol. Chem.* **396**, 465–482 (2015).
48. Connor, K. M. et al. Mitochondrial H2O2 regulates the angiogenic phenotype via PTEN oxidation. *J. Biol. Chem.* **280**, 16916–16924 (2005).
49. Yu, Q. et al. Mitochondrial hydrogen peroxide activates PTEN and inactivates Akt, leading to autophagy inhibition-dependent cell death in neuronal models of Parkinson's. *Dis. Mol. Neurobiol.* **60**, 3345–3364 (2023).
50. Cox, A. G., Winterbourn, C. C. & Hampton, M. B. Mitochondrial peroxiredoxin involvement in antioxidant defence and redox signalling. *Biochem J.* **425**, 313–325 (2009).
51. Ekoue, D. N., He, C., Diamond, A. M. & Bonini, M. G. Manganese superoxide dismutase and glutathione peroxidase–1 contribute to the rise and fall of mitochondrial reactive oxygen species which drive oncogenesis. *Biochim Biophys. Acta Bioenerg.* **1858**, 628–632 (2017).
52. Munro, D., Banh, S., Sotiri, E., Tamanna, N. & Treberg, J. R. The thioredoxin and glutathione-dependent H2O2 consumption pathways in muscle mitochondria: Involvement in H2O2 metabolism and consequence to H2O2 efflux assays. *Free Radic. Biol. Med.* **96**, 334–346 (2016).
53. Sheng, Y. et al. Comparison of two yeast MnSODs: mitochondrial Saccharomyces cerevisiae versus cytosolic Candida albicans. *J. Am. Chem. Soc.* **133**, 20878–20889 (2011).
54. Abreu, I. A. et al. The kinetic mechanism of manganese-containing superoxide dismutase from Deinococcus radiodurans: a specialized enzyme for the elimination of high superoxide concentrations. *Biochemistry* **47**, 2350–2356 (2008).
55. Greenleaf, W. B. et al. Role of hydrogen bonding in the active site of human manganese superoxide dismutase. *Biochemistry* **43**, 7038–7045 (2004).
56. Hearn, A. S. et al. Amino acid substitution at the dimeric interface of human manganese superoxide dismutase. *J. Biol. Chem.* **279**, 5861–5866 (2004).
57. Guan, Y. et al. Crystal structure of Y34F mutant human mitochondrial manganese superoxide dismutase and the functional role of tyrosine 34. *Biochemistry* **37**, 4722–4730 (1998).
58. Demicheli, V., Moreno, D. M. & Radi, R. Human Mn-superoxide dismutase inactivation by peroxynitrite: a paradigm of metal-catalyzed tyrosine nitration in vitro and in vivo. *Metallomics* **10**, 679–695 (2018).
59. Cabelli, D. E. et al. Role of tryptophan 161 in catalysis by human manganese superoxide dismutase. *Biochemistry* **38**, 11686–11692 (1999).
60. Hearn, A. S., Tu, C., Nick, H. S. & Silverman, D. N. Characterization of the product-inhibited complex in catalysis by human manganese superoxide dismutase. *J. Biol. Chem.* **274**, 24457–24460 (1999).
61. Bull, C., Niederhoffer, E. C., Yoshida, T. & Fee, J. A. Kinetic studies of superoxide dismutases: properties of the manganese-containing protein from Thermus thermophilus. *J. Am. Chem. Soc.* **113**, 4069–4076 (1991).
62. Valentine, J. S. & Curtis, A. B. A convenient preparation of solutions of superoxide aniom and the reaction of superoxide anion with a copper (II) complex. *J. Am. Chem. Soc.* **97**, 224–226 (1975).
63. Azadmanesh, J. et al. Revealing the atomic and electronic mechanism of human manganese superoxide dismutase product inhibition. *Nat. Commun.* **15**, 5973 (2024).
64. Leto, D. F. & Jackson, T. A. Mn K-edge X-ray absorption studies of oxo- and hydroxo-manganese(IV) complexes: experimental and theoretical insights into pre-edge properties. *Inorg. Chem.* **53**, 6179–6194 (2014).
65. Westre, T. E. et al. A multiplet analysis of Fe K-edge 1s → 3d pre-edge features of iron complexes. *J. Am. Chem. Soc.* **119**, 6293–6314 (1997).
66. Kroll, T. et al. Effect of 3d/4p mixing on 1s2p resonant inelastic x-ray scattering: electronic structure of oxo-bridged iron dimers. *J. Am. Chem. Soc.* **143**, 4569–4584 (2021).
67. Vance, C. K. & Miller, A. F. Novel insights into the basis for Escherichia coli superoxide dismutase's metal ion specificity from Mn-substituted FeSOD and its very high E(m). *Biochemistry* **40**, 13079–13087 (2001).
68. Braun, A. et al. X-ray spectroscopic study of the electronic structure of a trigonal high-spin Fe(IV) horizontal lineO complex modeling non-heme enzyme intermediates and their reactivity. *J. Am. Chem. Soc.* **145**, 18977–18991 (2023).
69. Leveque, V. J., Vance, C. K., Nick, H. S. & Silverman, D. N. Redox properties of human manganese superoxide dismutase and active-site mutants. *Biochemistry* **40**, 10586–10591 (2001).
70. Azadmanesh, J., Trickel, S. R. & Borgstahl, G. E. O. Substrate-analog binding and electrostatic surfaces of human manganese superoxide dismutase. *J. Struct. Biol.* **199**, 68–75 (2017).
71. Carrasco, R., Morgenstern-Badarau, I. & Cano, J. Two proton-one electron coupled transfer in iron and manganese superoxide dismutases: A density functional study. *Inorg. Chim. Acta* **360**, 91–101 (2007).
72. Abreu, I. A., Rodriguez, J. A. & Cabelli, D. E. Theoretical studies of manganese and iron superoxide dismutases: superoxide binding and superoxide oxidation. *J. Phys. Chem. B* **109**, 24502–24509 (2005).
73. Sheng, Y. et al. Six-coordinate manganese(3+) in catalysis by yeast manganese superoxide dismutase. *Proc. Natl Acad. Sci. USA* **109**, 14314–14319 (2012).
74. Bonetta Valentino, R. et al. The structure-function relationships and physiological roles of MnSOD mutants. *Biosci. Rep.* **42**, BSR20220202 (2022).
75. Andres, C. M. C., Perez de la Lastra, J. M., Andres Juan, C., Plou, F. J. & Perez-Lebena, E. Superoxide anion chemistry-its role at the core of the innate immunity. *Int. J. Mol. Sci.*, **24**, 1841 (2023).
76. Hamalainen, K., Siddons, D. P., Hastings, J. B. & Berman, L. E. Elimination of the inner-shell lifetime broadening in x-ray-absorption spectroscopy. *Phys. Rev. Lett.* **67**, 2850–2853 (1991).
77. de Groot, F. M. F., Krisch, M. H. & Vogel, J. Spectral sharpening of the Pt L edges by high-resolution x-ray emission. *Phys. Rev. B*, **66**, 195112 (2002).
78. Kroll, T. et al. Resonant inelastic X-ray scattering on ferrous and ferric bis-imidazole porphyrin and cytochrome c: nature and role of the axial methionine-Fe bond. *J. Am. Chem. Soc.* **136**, 18087–18099 (2014).
79. Solomon, E. I. Preface forum: functional insight from physical methods on metalloenzymes. *Inorg. Chem.* **44**, 723–726 (2005).

80. Azadmanesh, J., Trickel, S. R., Weiss, K. L., Coates, L. & Borgstahl, G. E. O. Preliminary neutron diffraction analysis of challenging human manganese superoxide dismutase crystals. *Acta Crystallogr F. Struct. Biol. Commun.* **73**, 235–240 (2017).
81. Whittaker, M. M. & Whittaker, J. W. Metallation state of human manganese superoxide dismutase expressed in Saccharomyces cerevisiae. *Arch. Biochem Biophys.* **523**, 191–197 (2012).
82. Lutz, W. E. et al. Perfect crystals: microgravity capillary counter-diffusion crystallization of human manganese superoxide dismutase for neutron crystallography. *NPJ Microgravity* **9**, 39 (2023).
83. Ng, J. D., Gavira, J. A. & Garcia-Ruiz, J. M. Protein crystallization by capillary counterdiffusion for applied crystallographic structure determination. *J. Struct. Biol.* **142**, 218–231 (2003).
84. Azadmanesh, J., Lutz, W. E., Coates, L., Weiss, K. L. & Borgstahl, G. E. O. Cryotrapping peroxide in the active site of human mitochondrial manganese superoxide dismutase crystals for neutron diffraction. *Acta Crystallogr F. Struct. Biol. Commun.* **78**, 8–16 (2022).
85. Kwon, H., Langan, P. S., Coates, L., Raven, E. L. & Moody, P. C. E. The rise of neutron cryo-crystallography. *Acta Crystallogr D. Struct. Biol.* **74**, 792–799 (2018).
86. Coates, L. et al. The macromolecular neutron diffractometer MaNDi at the spallation neutron source. *J. Appl Crystallogr* **48**, 1302–1306 (2015).
87. Coates, L., Stoica, A. D., Hoffmann, C., Richards, J. & Cooper, R. The macromolecular neutron diffractometer (MaNDi) at the spallation neutron source, oak ridge: enhanced optics design, high-resolution neutron detectors and simulated diffraction. *J. Appl Crystallogr* **43**, 570–577 (2010).
88. Arnold, O. et al. Mantid—Data analysis and visualization package for neutron scattering and μ SR experiments. *Nucl. Instrum. Meth A* **764**, 156–166 (2014).
89. Sullivan, B. et al. BraggNet: integrating Bragg peaks using neural networks. *J. Appl Crystallogr* **52**, 854–863 (2019).
90. Sullivan, B. et al. Improving the accuracy and resolution of neutron crystallographic data by three-dimensional profile fitting of Bragg peaks in reciprocal space. *Acta Crystallogr D. Struct. Biol.* **74**, 1085–1095 (2018).
91. Campbell, J. W. LAUEGEN, an X-windows-based program for the processing of Laue diffraction data. *J. Appl. Crystallogr.* **28**, 228–236 (1995).
92. Minor, W., Cymborowski, M., Otwinowski, Z. & Chruszcz, M. HKL-3000: the integration of data reduction and structure solution–from diffraction images to an initial model in minutes. *Acta Crystallogr D. Biol. Crystallogr* **62**, 859–866 (2006).
93. Afonine, P. V. et al. Towards automated crystallographic structure refinement with phenix.refine. *Acta Crystallogr D. Biol. Crystallogr* **68**, 352–367 (2012).
94. Garman, E. F. & Weik, M. Radiation damage in macromolecular crystallography. *Methods Mol. Biol.* **1607**, 467–489 (2017).
95. O'Young, C. & Lippard, S. J. Reactions of superoxide anion with copper(II) salicylate complexes. *J. Am. Chem. Soc.* **102**, 4920–4924 (1980).
96. McClune, G. J. & Fee, J. A. Stopped flow spectrophotometric observation of superoxide dismutation in aqueous solution. *FEBS Lett.* **67**, 294–298 (1976).
97. Kim, S., DiCosimo, R. & Filippo, J. S. Spectrometric and chemical characterization of superoxide. *Anal. Chem.* **51**, 679–681 (1979).
98. Newville, M. Larch: an analysis package for XAFS and related spectroscopies. *J. Phys.: Conf. Ser.* **430**, 012007 (2013).
99. Rehr, J. J., Kas, J. J., Vila, F. D., Prange, M. P. & Jorissen, K. Parameter-free calculations of X-ray spectra with FEFF9. *Phys. Chem. Chem. Phys.* **12**, 5503–5513 (2010).
100. Neese, F., Wennmohs, F., Becker, U. & Riplinger, C. The ORCA quantum chemistry program package. *J. Chem. Phys.* **152**, 224108 (2020).
101. Takano, Y. & Houk, K. N. Benchmarking the conductor-like polarizable continuum model (CPCM) for aqueous solvation free energies of neutral and ionic organic molecules. *J. Chem. Theory Comput* **1**, 70–77 (2005).
102. Weigend, F. & Ahlrichs, R. Balanced basis sets of split valence, triple zeta valence and quadruple zeta valence quality for H to Rn: Design and assessment of accuracy. *Phys. Chem. Chem. Phys.* **7**, 3297–3305 (2005).
103. Becke, A. D. Becke's three parameter hybrid method using the LYP correlation functional. *J. Chem. Phys.* **98**, 5648 (1993).
104. Neese, F. Prediction and interpretation of the 57Fe isomer shift in Mössbauer spectra by density functional theory. *Inorg. Chim. Acta* **337**, 181–192 (2002).
105. DeBeer George, S., Petrenko, T. & Neese, F. Prediction of iron K-edge absorption spectra using time-dependent density functional theory. *J. Phys. Chem. A* **112**, 12936–12943 (2008).
106. Roemelt, M. et al. Manganese K-edge X-ray absorption spectroscopy as a probe of the metal-ligand interactions in coordination compounds. *Inorg. Chem.* **51**, 680–687 (2012).

Acknowledgements

This research was supported by the NIH (R01-GM145647) and NASA EPSCoR (NE−80NSSC17M0030 and NE-NNX15AM82A) to G.E.O.B. The UNMC Structural Biology Core Facility was funded by the Fred and Pamela Buffett NCI Cancer Center Support Grant (P30CA036727). The research at Oak Ridge National Laboratory (ORNL) Spallation Neutron Source was sponsored by the Scientific User Facilities Division, Office of Basic Energy Sciences, US Department of Energy. The Office of Biological and Environmental Research supported research at ORNL Center for Structural Molecular Biology (CSMB) using facilities supported by the Scientific User Facilities Division, Office of Basic Energy Sciences, US Department of Energy. Use of the Stanford Synchrotron Radiation Lightsource (SSRL), SLAC National Accelerator Laboratory, is supported by the US Department of Energy (DOE), Office of Science, Office of Basic Energy Sciences under Contract DE-AC02-76SF00515. The SSRL Structural Molecular Biology Program is supported by the DOE Office of Biological and Environmental Research and by the National Institutes of Health, National Institute of General Medical Sciences (P30GM133894). The contents of this publication are solely the responsibility of the authors and do not necessarily represent the official views of NIGMS or NIH. Quantum chemical computations were completed using the Holland Computing Center of the University of Nebraska, which receives support from the Nebraska Research Initiative.

Author contributions

J.A. purified protein, performed X-ray/neutron crystallography and X-ray spectroscopy experiments, processed and analyzed data, performed quantum chemistry calculations, and wrote the manuscript. K.S., L.R.S., W.E.L., J.J.L., E.C., and M.D. purified protein, participated in data collection/refinement, helped make figures and performed instrument maintenance. S.K. and A.N. prepared superoxide solution and performed experiments. L.C., D.A.A.M., and K.W. performed neutron crystallography experiments and processed data. T.K. performed X-ray spectroscopy experiments, processed data, and performed quantum chemistry calculations. G.E.O.B. acquired funding, designed experiments, and participated in writing the manuscript.

Competing interests

The authors declare no competing interests.

Additional information

Supplementary information The online version contains supplementary material available at https://doi.org/10.1038/s41467-025-57180-3.

Correspondence and requests for materials should be addressed to Gloria E. O. Borgstahl.

Peer review information *Nature Communications* thanks the anonymous reviewer(s) for their contribution to the peer review of this work. A peer review file is available.